Interactions among Radiation, Convection, and Large-Scale Dynamics in a General Circulation Model

DAVID A. RANDALL,*,** HARSHVARDHAN,+,@ DONALD A. DAZLICH||,** AND THOMAS G. CORSETTI||,†

*Goddard Laboratory for Atmospheres, NASA/GSFC, Greenbelt, Maryland
+Department of Meteorology, University of Maryland, College Park, Maryland
|| Centel Federal Services Corp., NASA/GSFC, Greenbelt, Maryland

(Manuscript received 11 August 1988, in final form 4 January 1989)

ABSTRACT

We have analyzed the effects of radiatively active clouds on the climate simulated by the UCLA/GLA GCM, with particular attention to the effects of the upper tropospheric stratiform clouds associated with deep cumulus convection, and the interactions of these clouds with convection and the large-scale circulation.

Several numerical experiments have been performed to investigate the mechanisms through which the clouds influence the large-scale circulation. In the "NODETLQ" experiment, no liquid water or ice was detrained from cumulus clouds into the environment; all of the condensate was rained out. Upper level supersaturation cloudiness was drastically reduced, the atmosphere dried, and tropical outgoing longwave radiation increased. In the "NOANVIL" experiment, the radiative effects of the optically thich upper-level cloud sheets associated with deep cumulus convection were neglected. The land surface received more solar radiation in regions of convection, leading to enhanced surface fluxes and a dramatic increase in precipitation. In the "NOCRF" experiment, the longwave atmospheric cloud radiative forcing (ACRF) was omitted, paralleling the recent experiment of Slingo and Slingo. The results suggest that the ACRF enhances deep penetrative convection and precipitation, while suppressing shallow convection. They also indicate that the ACRF warms and moistens the tropical troposphere. The results of this experiment are somewhat ambiguous, however; for example, the ACRF suppresses precipitation in some parts of the tropics, and enhances it in others.

To isolate the effects of the ACRF in a simpler setting, we have analyzed the climate of an ocean-covered Earth, which we call Seaworld. The key simplicities of Seaworld are the fixed boundary temperature with no land points, the lack of mountains, and the zonal uniformity of the boundary conditions. Results are presented from two Seaworld simulations. The first includes a full suite of physical parameterizations, while the second omits all radiative effects of the clouds. The differences between the two runs are, therefore, entirely due to the direct and indirect effects of the ACRF. Results show that the ACRF in the cloudy run accurately represents the radiative heating perturbation relative to the cloud-free run. The cloudy run is warmer in the middle troposphere, contains much more precipitable water, and has about 15% more globally averaged precipitation. There is a double tropical rain band in the cloud-free run, and a single, more intense tropical rain band in the cloudy run. The cloud-free run produces relatively weak but frequent cumulus convection, while the cloudy run produces relatively intense but infrequent convection. The mean meridional circulation transports nearly twice as much mass in the cloudy run. The increased tropical rising motion in the cloudy run leads to a deeper boundary layer and also to more moisture in the troposphere above the boundary layer. This accounts for the increased precipitable water content of the atmosphere. The clouds lead to an increase in the intensity of the tropical easterlies, and cause the midlatitude westerly jets to shift equatorward.

Taken together, our results show that upper tropospheric clouds associated with moist convection, whose importance has recently been emphasized in observational studies, play a very complex and powerful role in determining the model results. This points to a need to develop more realistic parameterizations of these clouds.

1. Introduction

Clouds are much more than just swarms of radiatively active particles. As emphasized by Arakawa (1975), they are also associated with the release of latent heat, and with small-scale convective motions that accomplish major vertical redistributions of sensible heat, moisture, and momentum. Radiation, latent heating, and small-scale transports are of equal importance in the cloud–climate problem, and in fact

** Present affiliation: Department of Atmospheric Science, Colorado State University, Fort Collins, Colorado.
@ Present affiliation: Department of Earth and Atmospheric Sciences, Purdue University, West Lafayette, Indiana.
† Present affiliation: Science Applications Research Corp., Code 630.4, NASA/GSFC, Greenbelt, Maryland.

Corresponding author address: Dr. David A. Randall, Dept. of Atmospheric Science, Colorado State University, Ft. Collins, CO 80523.

these three cloud processes strongly interact with each other, as well as with the large-scale circulation.

General circulation models are now being used to predict the response of the climate to increased carbon dioxide concentrations and other perturbations. Deficiencies and uncertainties in current GCM cloudiness parameterizations are among the most serious obstacles preventing full confidence in the results of such climate forecasts (e.g., Schlesinger and Mitchell 1987; Wetherald and Manabe 1988).

Five basic questions concerning the role of clouds in climate can be arranged in a logical sequence:

1) *What is the distribution of cloudiness?* The International Satellite Cloud Climatology Project (ISCCP) is intended to provide observational answers to this question (Schiffer and Rossow 1983). We must also compare GCM-simulated cloudiness with observations. For the UCLA/GLA GCM, this task has been begun by Randall et al. (1985) and Harshvardhan et al. (1988; hereafter referred to as HRCD). The present paper builds on the results presented by HRCD.

2) *What processes generate the observed distribution of cloudiness?* This is the key problem addressed in the development of cloud parameterizations. Large-scale motions, surface fluxes, moist convection, and radiative cooling can all influence the distribution of cloudiness over the globe. Specific hypotheses concerning cloud generation processes must be tested against observations. This task is separate from that of comparing model-simulated and observed cloudiness, since such observations usually provide little or no quantitative information about the cloud generation processes. Section 2 gives a brief discussion of the cloud generation processes included in the UCLA/GLA GCM.

3) *What are the direct effects of the clouds on the radiation field?* A number of observational and theoretical studies have pointed to cloud-related radiative heating and cooling as an important forcing function for both large-scale circulations and deep cumulus convection (e.g., Webster and Stephens 1980). Ramanathan (1987) has termed these effects "cloud radiative forcing" (CRF). Measurements of the CRF at the top of the atmosphere are being provided through the Earth Radiation Budget Experiment (ERBE; Barkstrom et al. 1984), as well as several other satellite-based observational studies. The Earth radiation budget and CRF simulated by the UCLA/GLA GCM were discussed in part by HRCD; the present paper gives further discussion of the CRF, with emphasis on its vertical distribution in the atmosphere.

4) *What role do the clouds play in maintaining, regulating, or otherwise influencing the present climate?* This is the main subject of the present paper. To answer this question, it is necessary to show how the climate system responds to the CRF. The response is realized in part through interactions among radiation, convection, and the large-scale circulation. GCMs are ideal tools for investigating these interactions, through controlled numerical experiments.

5) *What role do the clouds play in climate change?* This is the problem of cloud feedback. Because the present paper does not deal with climate change, we do not address this question.

Section 2 summarizes the cloud generation processes included in the UCLA/GLA GCM, and presents results showing how these processes behave in actual simulations. Section 3 shows how the results respond to selected changes in the model's formulation. Section 4 isolates certain particularly interesting effects of the CRF over the oceans. Section 5 presents a summary and conclusions.

2. Cloud generation processes

As discussed by HRCD and in the Appendix, three types of clouds are generated by the UCLA/GLA GCM: optically thick convective "anvil" clouds, which horizontally fill a grid column from 400 mb to the highest level reached by the convection; supersaturation clouds, which occur when the relative humidity equals or exceeds 100%, are assigned a cloud fraction of 1, and have optical porperties that vary with temperature; and planetary boundary layer stratocumulus clouds, which can be arbitrarily thin, and are permitted to occur when there is a strong inversion at the PBL top. In this paper, we emphasize the effects of the upper-level supersaturation and anvil clouds that are associated with cumulus convection. The model's simulation of PBL stratocumulus clouds has been analyzed in detail by Randall et al. (1985).

Naturally enough, the parameterized cloud generation processes are closely coupled to certain aspects of the GCM's hydrologic cycle, especially the distribution of moisture itself and the intensity of moist convection. The model conserves moisture to machine accuracy; with 64-bit words, a one-day change of the globally averaged precipitable water agrees with the corresponding daily mean difference between evaporation and precipitation to about 10 digits. The observed atmosphere contains 23.8 mm of precipitable water in January and 27.7 mm in July (Trenberth 1981), while the simulated atmosphere contains only 22.5 mm in January and 25.3 mm in July. The simulated January and July mean distributions of precipitable water are shown in Fig. 1. Apart from a small negative bias, the model results are generally realistic in comparison with observations (e.g., Trenberth 1981; Prabhakara et al. 1985), showing maxima in a broad region including the equatorial western Pacific and the Bay of Bengal, and in smaller regions off the west coasts of Central America and in the tropical Atlantic. Considering that most of the water vapor is concentrated in the lowest 400 mb of the atmosphere, which is represented in the GCM by only three layers, the simulation is as realistic as can reasonably be expected. Only about 15% of the

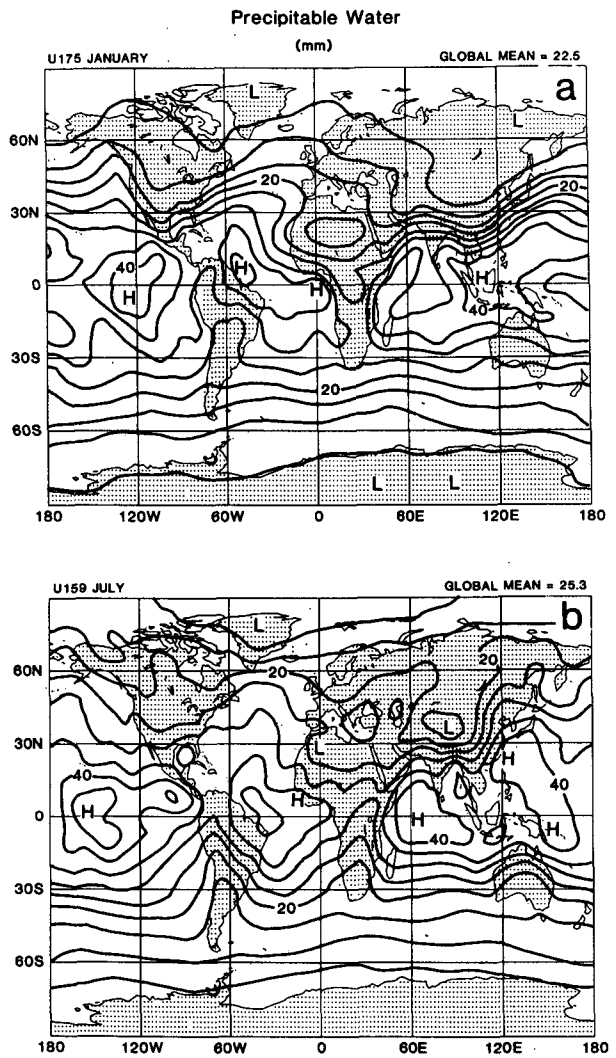

FIG. 1. Maps of the simulated January and July precipitable water. The contour interval is 5 mm.

model's water vapor is contained in the PBL; the remainder is supplied to the free atmosphere by the transport mechanisms described below.

The source of atmospheric water vapor is, of course, surface evaporation. This is regulated by the model's PBL parameterization, which features an explicit and highly variable PBL depth (Suarez et al. 1983). The PBL itself is identified as the lowest model layer. So long as moisture remains inside the PBL, it can only form PBL stratus clouds, which cannot become any deeper than the PBL itself. They have little effect on the outgoing longwave radiation at the top of the atmosphere, although they strongly influence both the solar and terrestrial radiation at the Earth's surface. In order to form either cumulus anvil clouds or large-scale saturation clouds in the free atmosphere, which are the main focus of attention in the present study, the moisture must find its way upward, out of the PBL. It cannot escape through vertical advection, because large-scale vertical motions lift the PBL top and the moisture together. The *only* ways that moisture can escape from the PBL into the free atmosphere are as follows.

1) Cumulus convection can draw mass, including moisture, out of the PBL. Much of the moisture that is carried up into the cumulus clouds is rained out, of course, but part of it is deposited into the free atmosphere by cumulus detrainment (Arakawa and Schubert 1974). As a result, the GCM produces cumulus drying at low levels and in the vertical mean, but cumulus moistening occurs near the top of the convective layer.

2) A collapse of the PBL due to a decrease in the rate of production of turbulence kinetic energy can leave moisture behind in the free atmosphere. This process is particularly important over strongly heated land, where there is a vigorous diurnal cycle of the PBL depth. During the day, turbulent entrainment causes the PBL to deepen, while surface evaporation maintains its high mixing ratio. As a result, its moisture content increases. Near sunset, the turbulent PBL collapses into a shallow near-surface layer. The deep moist layer that was generated during the day is still there, of course, but since it is no longer turbulent, it now resides within the free atmosphere. In this way, the diurnal deepening and shallowing of the PBL effectively pumps moisture into the free atmosphere, where it can be redistributed by advection and other processes. Of course, this diurnal pumping mechanism can lift water only as high as the highest level reached by the PBL top, which is constrained in the model to lie within about 180 mb of the Earth's surface.

3) Dry convective adjustment vertically redistributes both moisture and enthalpy when the lapse rate becomes dry convectively unstable. It affects the PBL only when very strong and persistent surface heating causes the PBL depth to reach its imposed upper limit. This frequently occurs over the Sahara Desert in the afternoon, for example. In such cases, dry convective adjustment essentially takes over and crudely represents a further deepening of the PBL beyond the artificially imposed limit. Model diagnostics show that this is a very minor term of the moisture budget.

4) The only other parameterized physical process that can transport moisture from the PBL into the free atmosphere is layer-cloud instability, which occurs in the model when the air just below the PBL top becomes saturated but the inversion is too weak to allow the presence of stratus cloud deck (Randall 1980; Suarez et al. 1983). This process tends to occur in association with cumulus convection, and its effects (Randall et al. 1985) are somewhat similar to those of the "shallow convection" parameterization in the ECMWF model (Tiedke 1985).

5) When spurious negative specific humidities occur, we redistribute moisture (without changing the total moisture content of the atmosphere) using a global multiplicative hole-filler (e.g., Rood 1987) that "borrows" moisture primarily from grid boxes where it is plentiful; such boxes naturally tend to be inside the PBL. Experiments show that the vast majority of "water holes" are produced by vertical advection. Although hole filling occurs far more often than we would like, its contributions to the moisture budget are, fortunately, very small.

For the free atmosphere above the PBL, the model does *not* include any parameterized vertical diffusion of moisture (or, for that matter, of potential temperature or momentum). Besides the processes already mentioned above, the *only* ways that moisture can be redistributed vertically in the model's free atmosphere are through large-scale vertical advection, parameterized moist convection that originates in the free atmosphere (discussed further below), and the evaporation of falling precipitation associated with large-scale condensation. Of course, this last process can only transport moisture downward.

When large-scale vertical motion is the primary mechanism for lifting moisture from the surface to the tropopause, high relative humidities occur throughout the tropospheric column. The model does produce such deep humid layers in middle latitudes, particularly in the winter hemisphere (Randall et al. 1985). In the model's tropics, however, high relative humidities near the tropopause are separated from the surface moisture supply by regions of low relative humidity in the middle troposphere. This indicates the importance of penetrative moist convective moisture transport for producing regions of high relative humidity and cloudiness in the upper tropical troposphere of the model.

The ultimate sink for atmospheric moisture is precipitation. The precipitation climatology of the current UCLA/GLA GCM is very similar to that presented by Randall et al. (1985), so it will be discussed only briefly here. Throughout the year, roughly two thirds of the simulated precipitation falls from cumulus ensembles, primarily in the tropics and the summer hemisphere; and the remaining third from large-scale saturation clouds, mainly in winter midlatitudes. Although the globally averaged simulated precipitation is substantially stronger than observed, its geographical distribution is fairly realistic. The GCM successfully produces the rainbands associated with the Atlantic and Pacific branches of the intertropical convergence zone, and also the heavy precipitation of the South Pacific convergence zone and the equatorial western Pacific. The simulated seasonally varying precipitation maxima for eastern North America, tropical Africa, tropical South America, and the Indian subcontinent are realistically positioned, but somewhat too strong. Further discussion is given by Randall et al. (1985).

Upper-level cloudiness in the model is always associated with one or more of three key parameterized processes. The first is penetrative cumulus convection that originates in the PBL. This is parameterized following Arakawa and Schubert (1974), as implemented by Lord et al. (1982). We refer to this parameterization as "CUP," for convenience. CUP represents the effects of cumulus clouds that originate at the PBL top. Although we expect this type of cumulus convection to be most important for driving the general circulation, it is also possible for cumulus updrafts to originate in the free atmosphere, above the PBL. For this reason, the GCM includes a supplementary parameterization for moist convection that originates above the PBL. This allows upper-level "altocumulus" convection to occur in the GCM, just as it does in the real atmosphere. It is parameterized in the GCM using Manabe's moist convective adjustment scheme. This adjustment, which we call "MSTADJ," is carried out in two steps. Convection is assumed to occur when the lapse rate exceeds its moist adiabatic value from one layer to the next, and saturation occurs in one or both of the layers; penetrative convection is not allowed. A mixing of mass is assumed to occur such that the lapse rate is restored to the moist adiabat, or saturation is eliminated, whichever occurs first. The mixing results in a highly supersaturated condition in the uppermost of the two layers in question. This supersaturation is then removed by the model's large-scale precipitation parameterization, which we call "LSP." The precipitation generated by LSP is assumed to evaporate into subsaturated layers that it encounters as it falls. These layers are moistened and cooled until they become saturated or the precipitation is exhausted, whichever occurs first. Of course, LSP is applied whenever supersaturation is detected, whether or not MSTADJ occurs. It follows that the frequency of occurrence of LSP exceeds that of MSTADJ. It is important to recognize that MSTADJ is applied only for pairs of layers that both lie *above* the PBL; cumulus convection that originates the PBL is parameterized exclusively through CUP.

Because the latent heating associated with MSTADJ is actually released by LSP, it is not accounted for in the MSTADJ heating diagnostic, but instead shows up as a portion of the LSP heating. For this reason, the MSTADJ heating diagnostic includes only the effects of *dry adiabatic* mass mixing, even though MSTADJ represents the effects of moist convection that is always accompanied by a release of latent heat. Of course, dry adiabatic mass mixing in the presence of a dry statically stable stratification leads to a warming below and a cooling above. This is seen in the MSTADJ heating diagnostic discussed below.

The GCM first determines the cumulus tendencies as parameterized by CUP, then checks for MSTADJ, and finally checks for LSP. It is quite common for all three of these processes to occur in the same grid col-

umn on the same time step. Although in nature all three occur simultaneously and in parallel, in the GCM the output from each parameterization is supplied as input to the next, in part to avoid raining out the same moisture more than once. The resulting interactions among CUP, MSTADJ, and LSP lead to some complex behavior by the model. Additional interactions involving radiation further complicate the results.

Simulated cloudiness in the free atmosphere is always associated with CUP, LSP, and/or MSTADJ. Cumulus convection that penetrates the 400 mb level is directly associated with anvil clouds, and indirectly tends to produce supersaturation clouds though detrainment moistening. LSP is always associated with supersaturation cloudiness. MSTADJ almost always occurs in conjunction with supersaturation clouds.

In the January and July mean results, CUP is only active over 9% of the Earth's surface, while MSTADJ is active over 17% of the Earth, and LSP over about 60%. Zonally averaged frequencies of occurrence are given as functions of latitude in Fig. 2. All three processes are active in a tropical belt that shifts to the north in July and to the south in January. The zonally averaged cumulus incidence reaches about 20% in the ITCZ, and has a secondary maximum over the northern continents in July. The cumulus anvil incidence (shown by HRCD) has nearly the same profile as cumulus incidence, but is slightly less frequent at each latitude. Although cumulus incidence and MSTADJ incidence increase and decrease together, MSTADJ is consistently more prevalent, even slightly so in the ITCZ. LSP occurs frequently at all latitudes, but is least active (around 50% of the time) in the subtropics. It has a strong maximum in middle latitudes in winter. Maps (not shown) indicate that all three processes are quite vigorous in the winter storm tracks east of North America and Asia, although most of the precipitation that reaches the Earth's surface there is generated by LSP rather than CUP.

Figure 3 shows the July-mean latitude–height cross sections of the zonally averaged heating due to CUP, MSTADJ, and LSP, as well as their sum, which we call the total latent heating. The January results are similar, once seasonal effects are accounted for, and are omitted for brevity. As shown in the figure, the zonally averaged cumulus heating has a maximum of more than 3 K day^{-1} at the 7 km level in the tropics, and a secondary maximum of about 1 K day^{-1} in the northern (summer) midlatitudes. Note, however, that the zonally averaged cumulus heating is actually negative near the tropopause. The reason is that cloud particles detrained from the cumuli lead to evaporative cooling and moistening near the cloud tops (Arakawa and Schubert 1974). As discussed in the next section, the upper tropospheric cumulus cooling disappears if the detrainment of cloud particles is artificially suppressed.

There are revealing relationships between the shapes

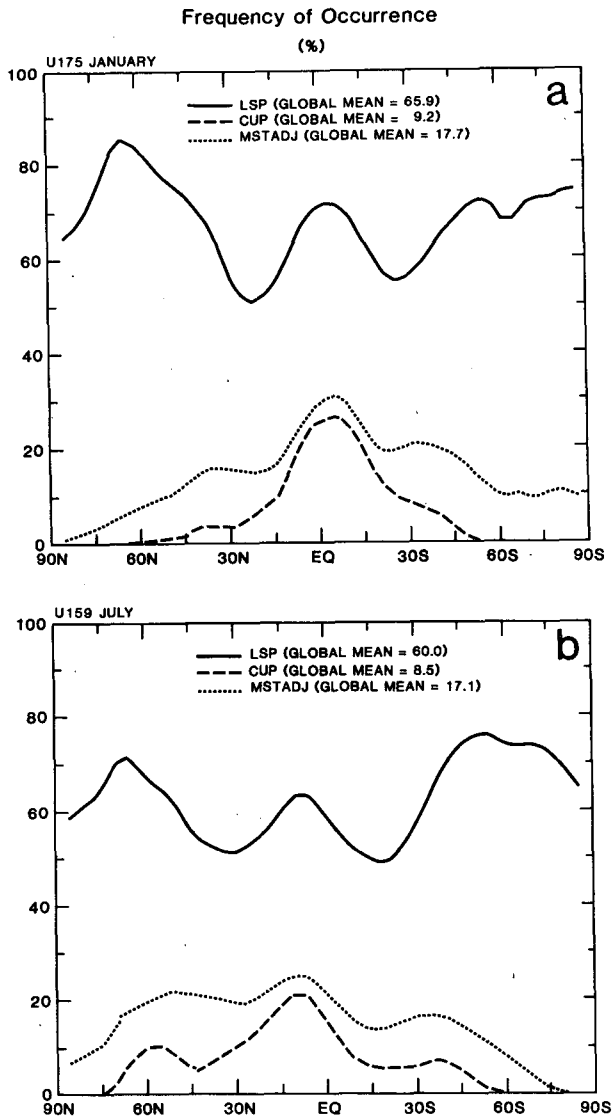

FIG. 2. Zonally averaged incidence of cumulus convection, large-scale saturation, and moist adjustment, in the July CONTROL simulation.

of the MSTADJ and LSP heating profiles, shown in Figs. 3b and 3c, respectively. Generally MSTADJ produces warming where LSP produces cooling, and vice versa; to a large extent they cancel each other out. This is to be expected if the sounding is close to a saturated moist adiabat. For the reason given earlier in this section, the MSTADJ diagnostic shows warming below and cooling above. There are centers of MSTADJ action in the middle tropical troposphere, and at lower levels in the midlatitudes. LSP produces zonally averaged heating maxima in excess of 2.5 K day^{-1} in three distinct regimes: the upper tropical troposphere, and the midlatitude middle troposphere of both hemispheres. Each of the three LSP heating maxima is ac-

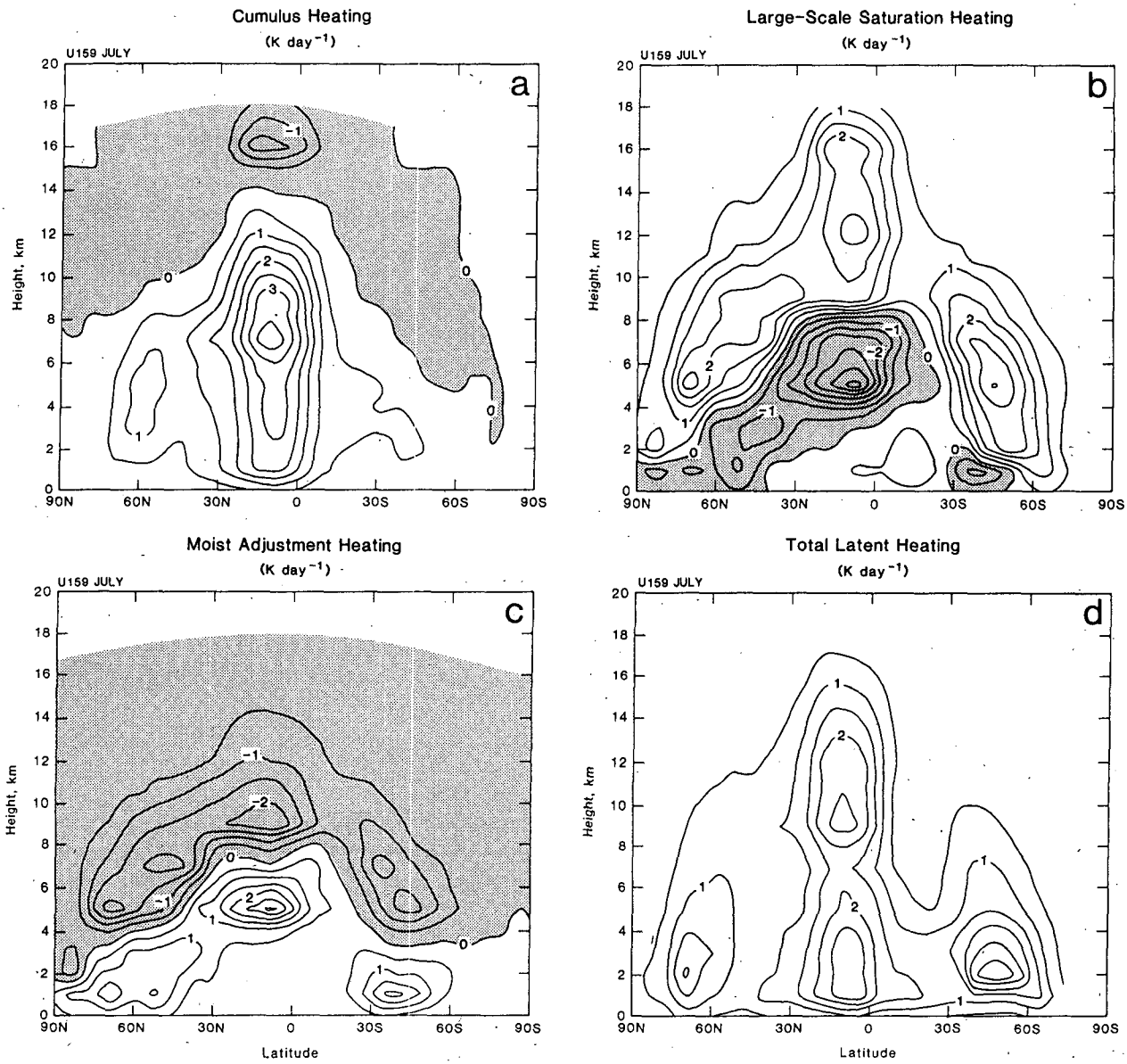

FIG. 3. For the July CONTROL simulation, latitude–height sections of (a) CUP heating, (b) MSTADJ heating, (c) LSP heating, (d) the sum of (a–c), which we call the total latent heating. In each panel, the contour interval is 0.5°K day^{-1}, and negative values are shaded.

companied by cooling at lower levels, where the falling precipitation evaporates. The zonally averaged cooling exceeds 3 K day^{-1} at the 5 km level at 10°N, and extends downward toward the north, continuously through the Northern Hemisphere subtropics. A small subtropical gap in the cooling occurs in the Southern Hemisphere. Although LSP produces only about half as much precipitation as CUP, the heating and cooling maxima associated with LSP are nearly as strong as those associated with CUP.

The combined effects of CUP, MSTADJ, and LSP can be called the total latent heating, and are shown in Fig. 3d. All coolings due to CUP, MSTADJ, and LSP have been canceled out by stronger warmings, leaving positive values of the total latent heating everywhere in the zonal mean, although of course this is not true locally. In particular, the zonally averaged cumulus cooling near the tropical tropopause has been canceled by LSP warming. Near 10°N, there is a deep maximum of the zonally averaged total latent heating, reaching up to about 17 km. Two maxima of about 2.5 K day^{-1} occur: one near 10 km, and a second between 1 and 4 km. A minimum at about 7 km separates the two maxima. This minimum total latent heating coincides approximately with the anvil cloud bases and the associated radiative warming. It is also near the

level where the cumulus heating is strongest! Additional maxima of the total latent heating occur at low levels near 45°S, 70°N. CUP contributes very little to the winter (Southern Hemisphere) maximum, but quite substantially to the summer (Northern Hemisphere) maximum. These results show that the cumulus heating and the total latent heating are quite different, even in the tropics.

The interactions among CUP, MSTADJ, and LSP in the tropical upper troposphere are particularly interesting. The cooling and moistening due to cumulus detrainment often lead to large-scale saturation, and also to moist convective instability between neighboring model layers. In such cases, both LSP and MSTADJ are driven into action by CUP. The upper-tropospheric moist convection is further invigorated by the effects of longwave radiation, which cools near the tops of the anvils, and warms at their bases. These important radiative effects are discussed in more detail later.

It appears that MSTADJ, which was expected to be relatively unimportant in the model, actually plays a significant role. Potentially destabilizing processes that may be responsible for forcing the vigorous MSTADJ activity include large-scale motions, radiative destabilization associated with upper-level stratiform clouds, and cooling due to the evaporation of the precipitation falling from such clouds. Further discussion of the MSTADJ forcing is given in section 3 below.

Both LSP and MSTADJ come into play in the vast majority of cases for which CUP produces deep convection. Experiments in which the serial order of CUP, MSTADJ, and LSP is modified show significant sensitivity of the model results to the order assumed. This is disturbing, since little or no a priori justification can be given for any particular order. In many cases when CUP is active, LSP and MSTADJ are merely extensions of the cumulus parameterization; the heating and drying due to LSP and MSTADJ are then essentially controlled, on very short time scales, by the cumulus mass flux.

The same can be said of the radiative effects of cumulus cloudiness, since the simulated convection also interacts strongly and on short time scales with the radiation parameterization. Figure 4 shows the simulated latitude–height distributions of the zonally averaged solar, terrestrial, and total ACRF, for the January simulation. (Unfortunately, these diagnostics are not available for the June–July simulation.) The zonally averaged solar ACRF is virtually negligible, apart from a 0.4 K day^{-1} warming in the upper tropical troposphere. Weak negative solar ACRF occurs at low levels in the tropics and the Northern Hemisphere, and is due to decreased gaseous absorption of solar radiation in the shadows of upper-level clouds. The dominant terrestrial CRF has three main features. At low levels in midlatitudes, strong cooling occurs in association with low-level cloud tops. In the tropics, there is a warming of about K day^{-1} at the 7 km level, and a cooling of about 1 K day^{-1} at 16 km. This strong radiative "dipole" is the signature of the optically and geometrically thick convective anvil clouds, which warm near their bases and cool near their tops (Ackerman et al. 1988). By cooling aloft, the anvils tend to destabilize the upper troposphere, favoring deep convection; at the same time, by warming the middle troposphere they tend to suppress convective elements that would otherwise terminate there. This evidence for cloud-induced radiative destabilization of deep convection bolsters the suggestion of HRCD that the ACRF feeds back positively on the processes that generate upper-level cloudiness. Further discussion is given later.

Our GCM results can be compared with the high-resolution numerical simulations of upper-tropospheric layer clouds by Starr and Cox (1985a,b). They find that such cloud layers are strongly convective, especially at night. The convection is most vigorous for optically thick clouds, and is driven partly by the vertical profile of the longwave radiative heating/cooling, and partly by latent heat effects. We do not claim that these effects are realistically simulated by the parameterizations of the current GCM; at best, they are qualitatively mimicked. Together, MSTADJ and LSP crudely represent a layer cloud undergoing turbulent convection that is nonpenetrative on the vertical scales resolved by the GCM. Radiative cooling near the cloud tops and warming near the cloud bases promotes the convection. This is the crude but recognizable way that a current-generation GCM represents cirrus and/or anvil cloud processes.

3. Some numerical experiments

In this section, we report on the results of three numerical experiments designed to reveal some of the interactions among the various parameterized physical processes of the GCM.

The first experiment deals with the effects of the detrainment of cloud particles from cumulus updrafts. According to Arakawa and Schubert (1974), cumulus clouds modify their environment in part by detraining cloud air near their tops. The detrained air, which may contain liquid water and/or ice as well as water vapor, becomes part of the environment at the cloud-top level. Detrainment therefore tends to moisten the environment, and also to cool it if the detrained condensate is converted back to vapor. Upper-level cloudiness can therefore increase as a result of detrainment, either because the detrained cloud material itself forms an extended cloud, or because cooling and moistening promote an increase in the relative humidity at the detrainment level. The second mechanism is included in the current UCLA/GLA GCM, but the first mechanism is not.

In both of the CONTROL runs described by HRCD, a part of the liquid water and ice condensed in cumulus

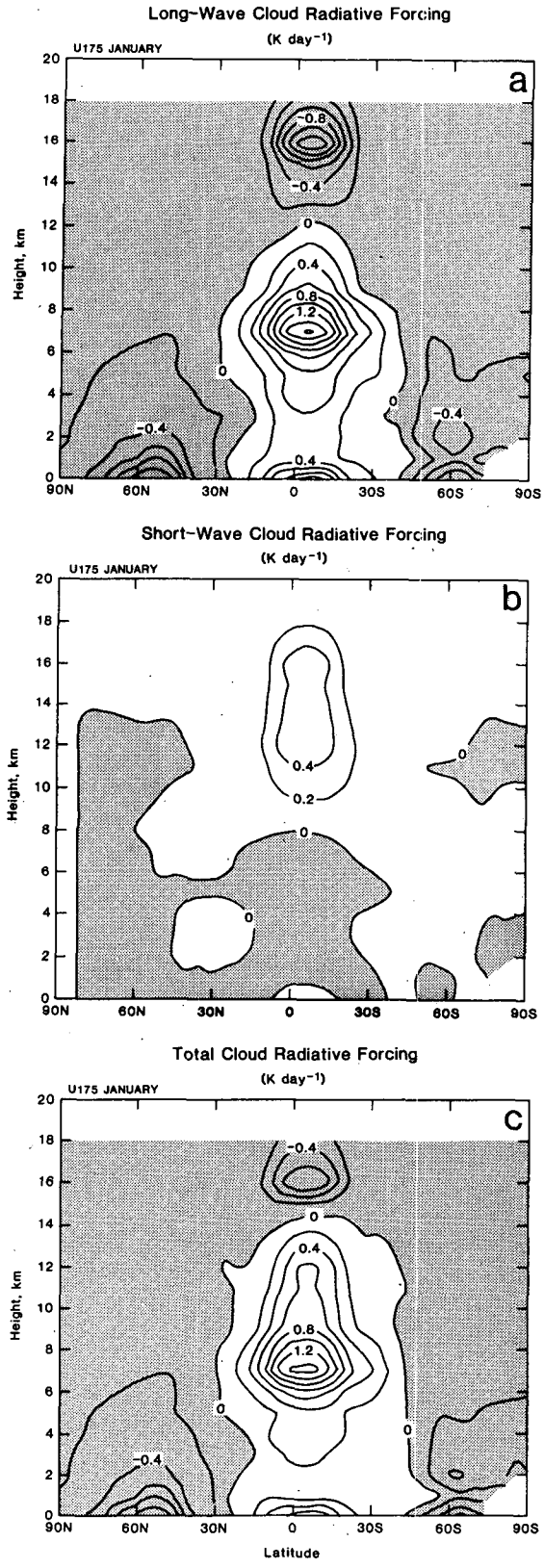

FIG. 4. The simulated latitude–height distributions of the zonally averaged solar, terrestrial, and total ACRF, for the January CONTROL simulation. In each panel, the contour interval is 0.5 K day^{-1}, and negative values are shaded.

clouds was allowed to detrain and moisten the environment, at every level. As discussed by Houze (1977, 1982), observations show that a major fraction of the condensate detrained by cumulus towers precipitates to lower levels of the atmosphere or even to the surface. This precipitation falls from anvil clouds that attain mesoscale proportions. Realistic anvils would not typically be large enough to fill a grid box of the current UCLA/GLA GCM, however, so the large-scale precipitation parameterization of the current GCM may be incapable of realistically simulating anvil cloudiness and precipitation. Based on this line of reasoning, Lord et al. (1982) suggested that, as a first approximation, *all* of the liquid water and ice condensed in cumulus clouds above 500 mb should be rained out. We tested this suggestion in a 60-day June–July experiment which we call "NODETLQ." We analyzed the last 30 days of the run, which was started from initial conditions matched with those of the June–July CONTROL run. The purpose of the NODETLQ experiment is to investigate the sensitivity of the model to cumulus detrainment of cloud particles.

Figure 5 shows the zonally averaged cumulus heating profile in the experiment and control, as well as the difference. These changes can be thought of as the forcing for this experiment. In the control run, the zonally averaged cumulus heating becomes negative above about 14 km in the tropics, and above 10 km over the Northern Hemisphere continents. These negative values are due to cumulus detrainment and the subsequent evaporation of cloud condensates. In the experiment, no such negative cumulus heating rates occur. Tropical deep convection weakens, but shallow convection intensifies. In the control, large-scale supersaturation is very active between 9 km and 17 km in the tropics, and between 2 and 10 km in the northern midlatitudes. It is caused primarily by moistening and cooling due to the evaporation of cloud particles detrained from cumulus clouds. In the experiment, there is practically no upper-level large-scale saturation in the tropics, and very little in the Northern Hemisphere. The vigorous tropical MSTADJ activity of the control, evident in Fig. 3, is also greatly reduced in the experiment, although the midlatitude MSTADJ activity is almost unchanged. This indicates that destabilization produced by the cooling associated with detrained cloud particles in the upper tropical troposphere is the primary forcing mechanism for MSTADJ in the model tropics. We strongly suspect that this destabilization is exaggerated in the model.

Figure 6 shows the zonally averaged total latent heating profile in the experiment and control, as well as the difference. There is less latent heating above 8 km in the experiment, but there is more between 4 and

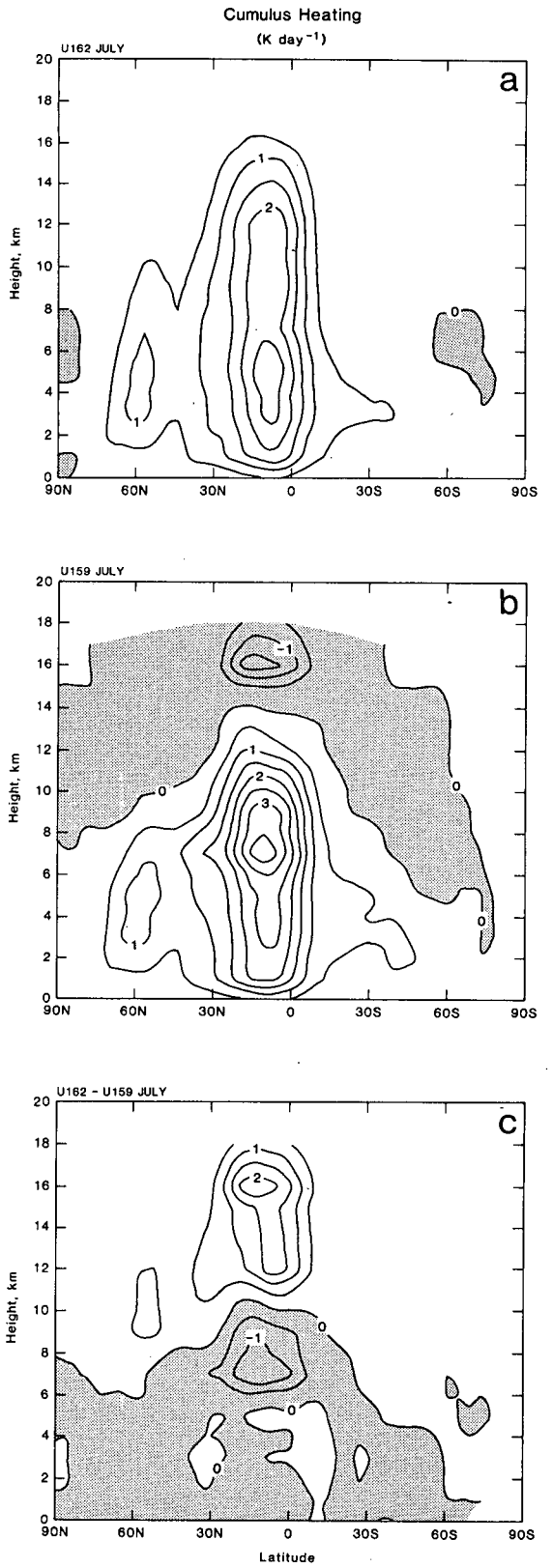

FIG. 5. Zonally averaged cumulus heating for (a) NODETLQ, (b) control, (c) the difference.

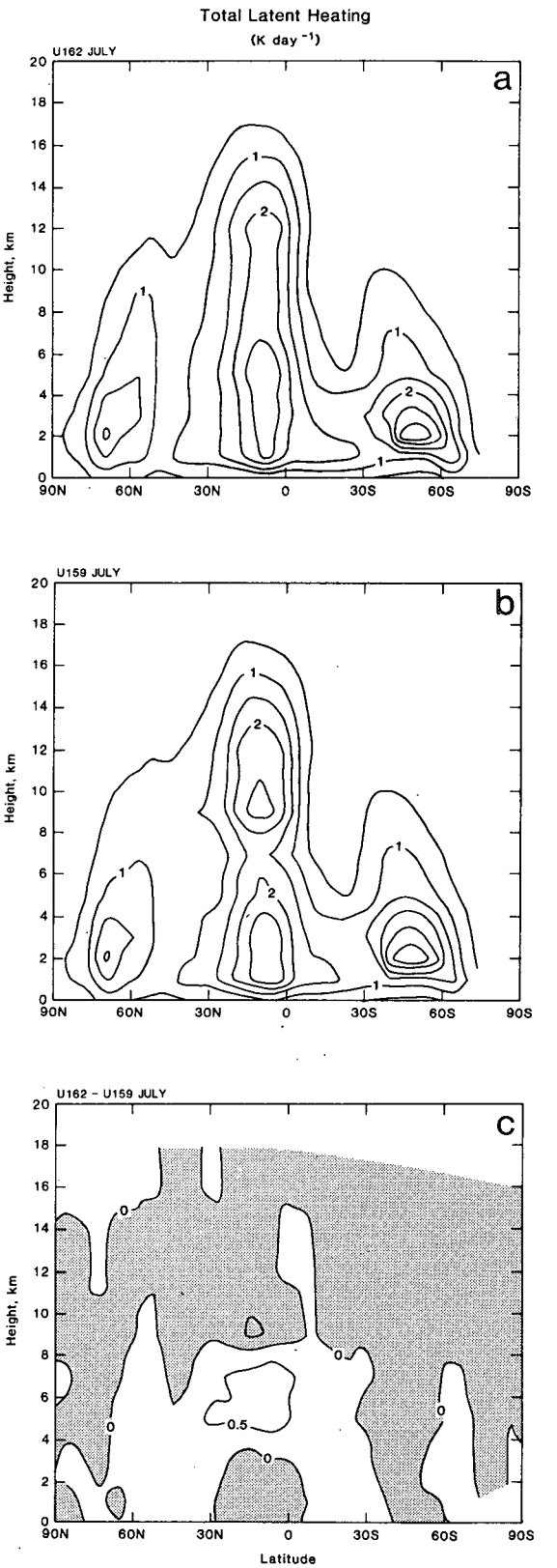

FIG. 6. Zonally averaged total latent heating for (a) NODETLQ, (b) control, (c) the difference.

8 km. The experiment has much less upper-level cloudiness (Fig. 7). Total cloudiness and high (above 400 mb) cloudiness each decrease by 4%. The precipitable water content of the atmosphere decreases by 1.5 mm globally and 4 mm in the tropics (Fig. 8). The tropical OLR increases by about 15 W m^{-2}.

The NODETLQ experiment demonstrates that, in the GCM, the detrainment of cloud particles from cumulus towers plays a significant role in the interaction between convection and radiation in the tropics. It also shows that the model is quite sensitive to the current, somewhat arbitrary coupling of CUP, MSTADJ, and LSP. This indicates that we need a more sophisticated coupling of the cumulus and large-scale precipitation processes, together with an improved parameterization of cumulus convection that originates above the PBL.

The second experiment deals with the effects of the cumulus anvils. As discussed by HRCD, in the current model, cumulus clouds are assumed for simplicity to have negligible cloud fraction below 400 mb. When convection penetrates above 400 mb, however, an optically thick anvil cloud is assumed to cover the grid, from 400 mb to the highest level reached by the convection. To the extent that this admittedly highly arbitrary parameterization of cumulonimbus anvil cloudiness influences the model's climate, a model development effort is required to provide a more realistic and physically based parameterization. In the second experiment, we investigated this possibility by neglecting the effects of the anvil clouds in both the longwave and shortwave radiation parameterizations. The cloud fraction for convective clouds was, therefore, set to zero at all levels. A June–July simulation was performed.

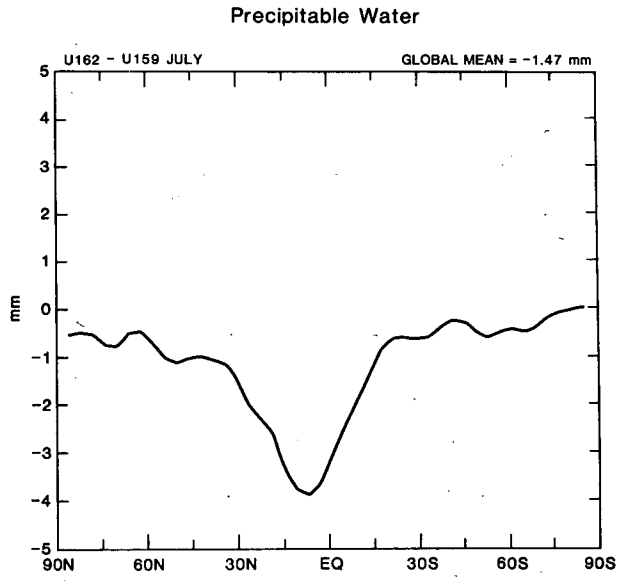

FIG. 8. Change in zonally averaged precipitable water between NODETLQ and control.

The results show a dramatic decrease in high cloudiness, as indicated in Fig. 9; this is, of course, directly due to the removal of the anvils, and can be interpreted as the forcing for this experiment. The greatest decrease in cloudiness is near 10°N, but there is a second strong decrease near 50°N. The former is associated with the ITCZ, primarily over the oceans, while the latter is associated with convection over the warm continents of the Northern Hemisphere.

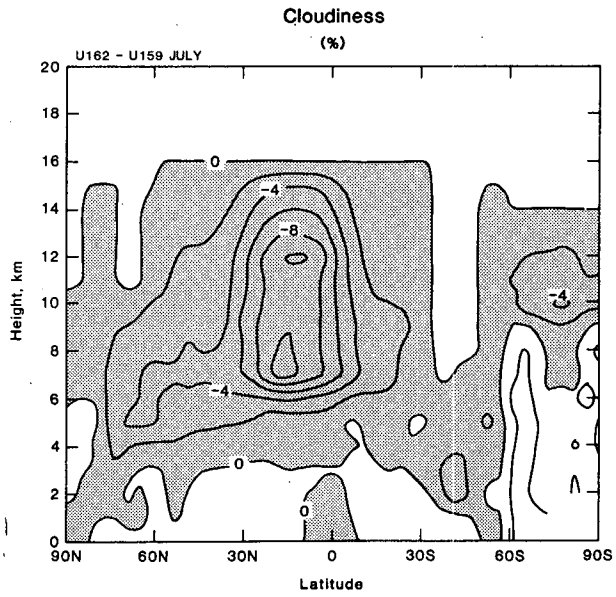

FIG. 7. Change in zonally averaged cloudiness between NODETLQ and control.

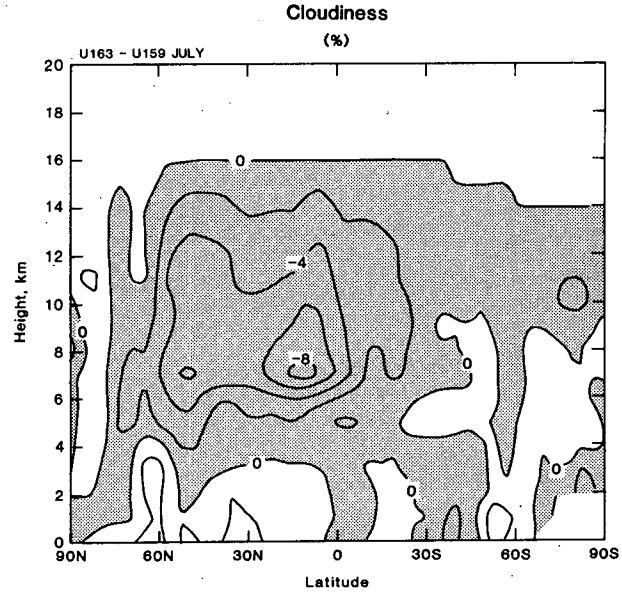

FIG. 9. Change in zonally averaged cloudiness between NOANVIL and control.

As a result of the reduced anvil cloudiness, the simulated planetary albedo decreases to a very unrealistic 24%. The OLR increases by only 7 W m^{-2} in the global mean, but it increases by about 50 W m^{-2} in convectively active regions, and by 20 W m^{-2} in the zonal mean at 10°N. The tropical minimum of the zonally averaged OLR becomes less pronounced, although a weak minimum still occurs because of plentiful water vapor and supersaturation cloudiness.

The globally averaged surface solar radiation increases by 16 W m^{-2}, and of course most of the increase is concentrated in regions that are prone to deep convection. The removal of the anvils has very different effects over land and ocean. For the land points of the model, the increased insolation leads to an increase in the surface sensible and latent heat fluxes. This causes the globally averaged surface latent heat flux to increase by 7 W m^{-2}. The precipitable water content of the atmosphere increases in response to the increased evaporation. In contrast, the portion of the increased surface solar radiation that enters the oceans naturally has no effect on the results of our simulation, due to our use of prescribed sea surface temperatures. Later in this paper we present much further discussion of the contrasting effects of the CRF over land and ocean.

Figure 10 shows that the longwave cooling is reduced at and above the mean level of the tropical anvils, and increased near the anvil cloud base level. There is also a slight decrease in the solar heating at the levels of the anvils. Note that there are no corresponding features in the longwave cooling difference at 50°N, even though, as shown in Fig. 9, the anvil cloudiness has decreased there too. The reason for this is explained below.

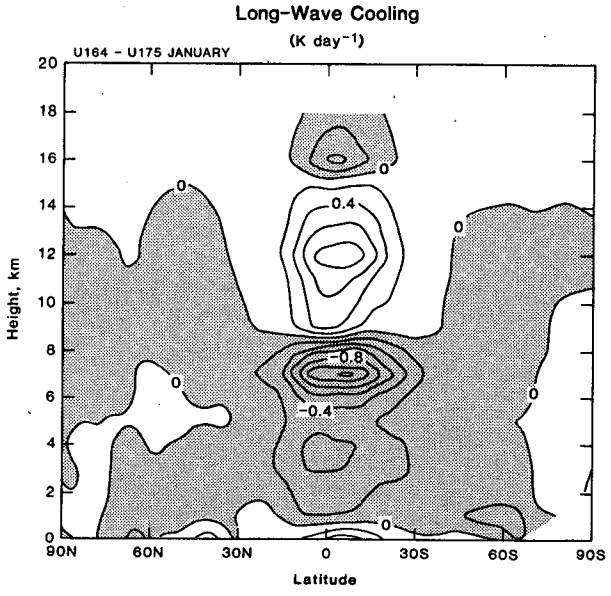

FIG. 10. Change in zonally averaged longwave cooling rate between NOANVIL and control.

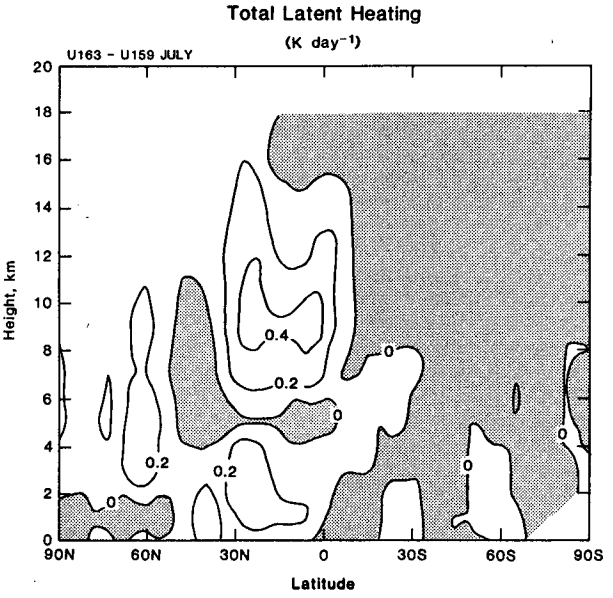

FIG. 11. Change in zonally averaged total latent heating between NOANVIL and control.

Neither convective nor large-scale precipitation is affected appreciably in the global mean, although the total precipitation rate increases slightly. Figure 11 shows that the total latent heating increases in the tropics, particularly near the 8 km level, where the longwave cooling has increased. The radiative and latent heating changes tend to compensate for each other in this region; in fact, it appears that over the tropical oceans the change in the latent heating is a response to the change in the radiative cooling. Near 60°N, there is a weaker and shallower increase of the latent heating in response to removing the anvils.

The situation is different over the Northern Hemisphere continents. Near 50°N, convective activity increases, primarily over land; the absence of cloud shadows allows increased surface sensible and latent heating, which tend to destabilize the atmosphere with respect to cumulus convection. Because of the nature of this experiment, the enhanced convection cannot make any direct contribution to the cloud cover. A negative feedback loop is suggested, however; over land, removing the anvils promotes deep convection, which would favor the formation of anvils. Another way of describing this result is that the surface cloud radiative forcing (CRF) associated with the anvils acts to suppress the convection that produces the anvils. This indicates the existence of a negative feedback loop: convection produces cloudiness, which reduces surface evaporation, which tends to slow down the convection. Further discussion of this point is given later in this paper.

Figure 12 shows the dramatic changes in temperature. There is a pronounced warming throughout the

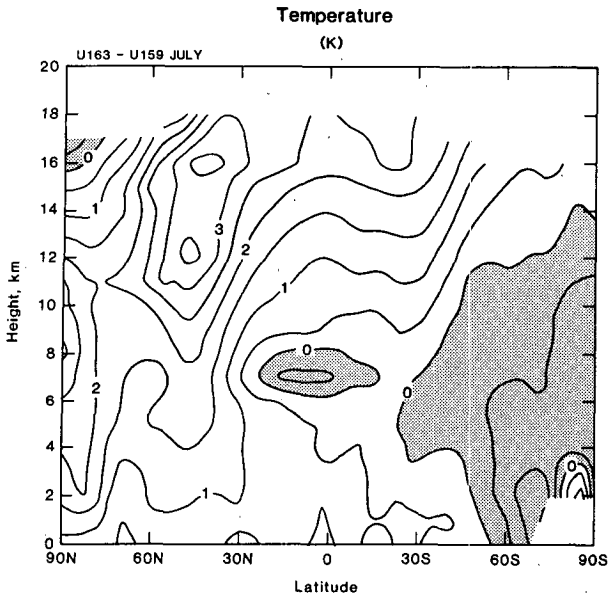

FIG. 12. Change in zonally averaged temperature between NOANVIL and control.

troposphere in the northern midlatitudes, increasing with height and reaching 3.5°K in the upper troposphere. Moeng and Randall (1982) obtained a similar result in an experiment with an earlier Goddard GCM. This temperature increase cannot be explained directly in terms of the changes in the radiative or latent heating fields (cf. Figs. 8 and 10). The vertical structure of the warming represents a decrease in the lapse rate of temperature and tends to inhibit moist convection. In the same region, the precipitable water increases by about 2 mm, as a result of the increased surface latent heat flux. This moistening of the column tends to promote moist convection. The changes in the temperature and moisture thus have opposing effects on the conditional stability of the atmosphere. Our interpretation is that the increase in the temperature aloft is produced by the model in order to prevent the conditional instability from increasing in response to the moistening of the column. The Arakawa–Schubert cumulus parameterization used in the GCM tends to have just this effect; there is also observational evidence for the existence of such negative correlations between the lapse rate of temperature and the low-level humidity in convectively active regions (Arakawa and Chen 1987).

Note that the reduced upper tropospheric cloudiness at 50°N does *not* lead to a decrease in the longwave cooling rate there. This is understandable in view of the increased temperature, which favors stronger cooling and so tends to compensate for the reduced cloudiness.

Removing the anvils modifies the CRF so as to warm the planet by 8 W m^{-2}, due to increased absorption of solar radiation; but the change in the *atmospheric* CRF tends to *cool* the atmosphere by -5 W m^{-2}, due to increased emission of terrestrial radiation; the planetary warming is felt at the Earth's surface. This causes an increase in the temperature of the continental land surfaces, which leads to a warming of the atmosphere. The increased flux of energy from the continents to the atmosphere is balanced by the enhanced radiative cooling of the atmosphere that results from the removal of the anvils. This again illustrates the great importance of the cloud radiative forcing of the Earth's surface. Even though the present model has fixed sea surface temperatures, and even though the removal of the anvils actually reduces the radiative energy input to the atmosphere, the warming of the continents due to the increased surface solar radiation actually leads to a warming of the atmosphere. If the sea surface temperatures were free to increase in the model, the surface CRF would presumably be even more effective in regulating the atmospheric temperature.

The third experiment deals with the effects of the atmospheric cloud radiative forcing (ACRF). The vertical integral of the atmospheric cloud radiative forcing obtained with the UCLA/GLA GCM, which is presented by HRCD, is similar to that obtained by Slingo and Slingo (1988, hereafter S^2) with the NCAR Community Climate Model (CCM). This agreement is somewhat misleading, however, because the latitude–height distribution of the ACRF shown in Fig. 4 differs dramatically from that obtained with the CCM. The most important differences are in the tropics, where the UCLA/GLA GCM produces strong cooling near the tropopause and strong warming near 400 mb, while the CCM gives weak warming throughout the troposphere above 600 mb.

These differences in the simulated ACRF are related to the differences in the cloud generation schemes and cloud optical properties of the two models. Both models produce a combination of optically thin cirrus and optically thick anvil clouds in the upper tropical troposphere. In the CCM, the convective cloud fraction in each layer is assumed to be $0.35/N$ where N is the number of layers undergoing convection. Random overlap is assumed. In addition, deep convective clouds in the CCM are assumed to be capped by an optically thick cirrus shield one sigma layer thick, with cloud fraction 0.95. These assumptions combine to produce weak radiative warming through the depth of the cloud layer, and to prevent any radiative cooling at the cloud top level. In contrast, as discussed in section 2 and by HRCD, the anvils of the UCLA/GLA model are assumed to fill the grid boxes, from 400 mb to the highest level reached by the convection, which in the tropics is typically near the tropopause. The effects of the anvils in the UCLA/GLA GCM have already been discussed above; it is clear that they are primarily responsible for the vertical distribution of the ACRF shown in Fig. 4.

This comparison of results between the two models shows the importance of investigating the vertical dis-

tribution of the ACRF inside the atmosphere, rather than simply focusing on its vertical integral. It also shows the importance of the vertical distribution of cloudiness, in addition to the "total cloudiness" (one minus the fraction of clear sky) so often discussed in the literature.

Slingo and Slingo performed an experiment with the CCM in which the longwave ACRF was artificially suppressed; clear-sky cooling rates were used to predict the atmospheric temperature, while the usual (clear and cloudy) longwave flux was used to predict the land-surface temperature. January conditions were chosen on the grounds that the land-surface is minimally sensitive to longwave ACRF in northern winter. The results of the CCM experiment can be summarized as follows: the ACRF warms the tropical upper troposphere by 4 K and cools the tropical lower stratosphere by 6 K, causing an acceleration of the subtropical jets in both hemispheres. The tropical 200 mb heights increase by more than 100 m, and a "PNA" pattern is evident in a map of the 200 mb height difference between the experiment and the control. The ACRF also leads to a moistening of the tropical middle troposphere by invigorating moist convection, which transports moisture upwards. This moistening reaches about 1 g kg^{-1} in the zonal mean at 850 mb. The enhanced moist convective activity is mainly confined below the 700 mb level. The ACRF causes increased precipitation and large-scale rising motion over Indonesia, and S^2 conclude that it tends to increase the precipitation rate in regions where precipitation is likely to occur anyway. They also conclude that much of the effect of ACRF on the large-scale circulation is produced indirectly; the ACRF modifies the latent heating, and the ACRF and latent heating together modify the large-scale circulation.

We have performed an analogous experiment with the UCLA/GLA GCM, to determine to what extent the results of S^2 are model-dependent. The CCM and the UCLA/GLA GCM differ in many ways, notably in their cloud-radiation parameterizations, cumulus parameterizations, and discretization schemes. As discussed above, the two models produce very different vertical distributions of the ACRF. The following discussion shows that there are both similarities and differences between our results and those of S^2, although there is little basis to conclude that either set of model results is "right" or "wrong."

Figure 13 shows the change in the longwave cooling of the atmosphere between the NOCRF experiment and the control. (For the experiment, the cooling is just the clear-sky value, while for the control it is the clear/cloudy value. Note that we are plotting the experiment minus the control; the effects of the ACRF are *minus* the differences shown in the figure.) The change in the longwave cooling is the forcing for this experiment, and corresponds closely to (minus) the ACRF in the control run. The ACRF leads to a decrease

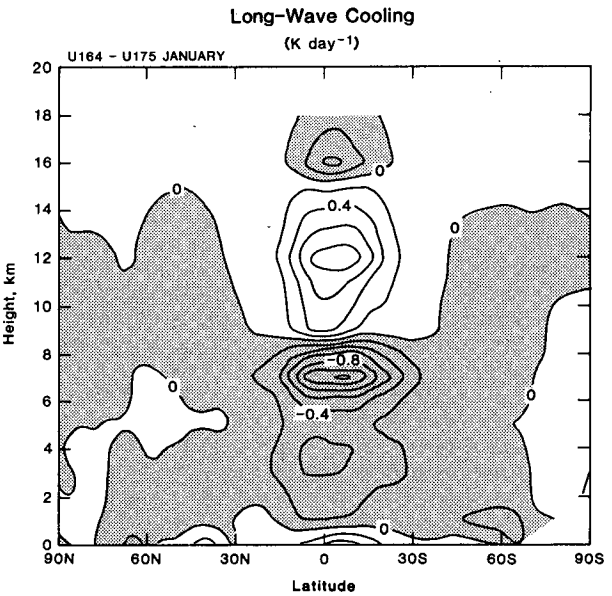

FIG. 13. Zonally averaged change in the longwave cooling of the atmosphere between the NOCRF experiment and the control.

in the longwave cooling rate by more than 1 K per day at the 7 km level (near 400 mb) in the tropics, and to an increase of more than 1 K per day near the tropical tropopause. These results differ dramatically from those obtained with the CCM by S^2, simply because the CCM produces a very different vertical distribution of longwave ACRF, featuring warming throughout the upper tropical troposphere, with cooling centered near 850 mb. The deep warming is presumably associated with the effects of optically thin or highly variable clouds that absorb upwelling longwave radiation from the surface, while the cooling must be due to the common occurrence of cloud tops near 850 mb. The UCLA/GLA GCM produces concentrated warming near 400 mb, where the anvils absorb upwelling longwave radiation, and concentrated cooling near 200 mb, where anvil tops frequently occur.

These radiative perturbations have a very strong impact on the simulated moist convection. As shown in Fig. 14, tropical convection penetrates to the 17 km level in the control, but is largely confined below 12 km in the experiment. On the other hand, below the 8 km level, the tropical cumulus heating, shown in Fig. 14c, is suppressed by the ACRF. This appears to be a response to the decreased longwave cooling at about the same level (refer to Fig. 13). The ACRF also acts to increase the cumulus heating between 8 and 14 km, and to enhance detrainment cooling near the tropopause. The ACRF leads to a decrease in the total latent heating (Fig. 14d) at 7 km, where the clouds act to reduce the longwave cooling, but the total latent heating increases both above and below the 7 km level.

Whereas S^2 found that the ACRF enhances low-level

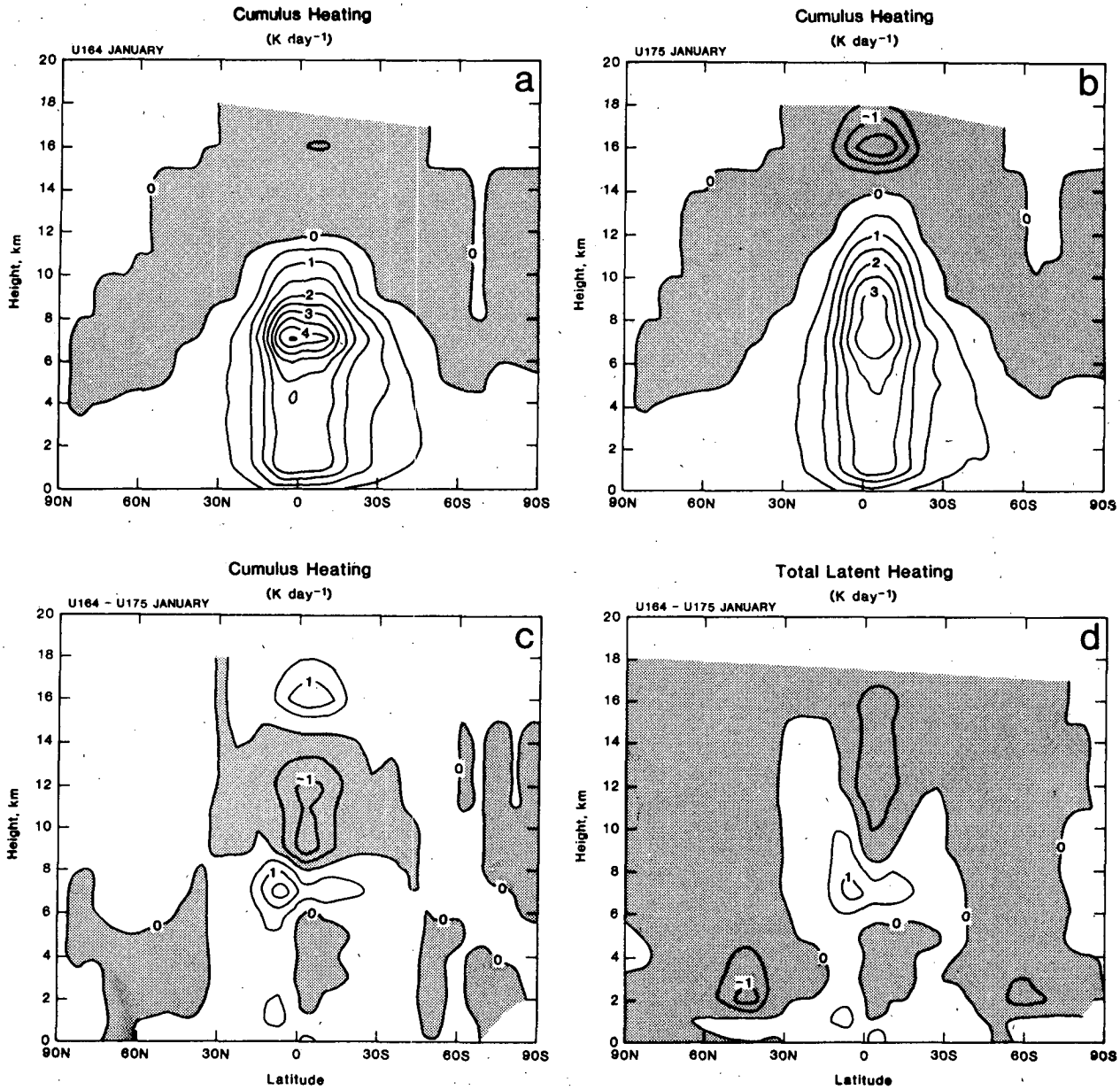

FIG. 14. Zonally averaged cumulus heating for (a) the NOCRF experiment, (b) the control, and (c) the difference. Panel (d) shows the difference in the zonally averaged total latent heating between the NOCRF experiment and the control.

moist convective activity, in our experiment the low-level convection is actually suppressed, and deep convection is enhanced. One possible explanation is that in the UCLA/GLA GCM, the intensification of the deep convection is due in part to the strong radiative cooling at the anvil cloud tops, which induces deep penetrative convection by destabilizing the upper troposphere with respect to the surface air. A second factor is the tendency of the CRF to warm the atmospheric column as a whole in regions of deep convection. This favors large-scale rising motion, which can in turn promote deep moist convection. Further discussion is given later.

Although the globally averaged total precipitation rate is practically unchanged in the experiment, there are very strong regional responses, as shown in Fig. 15. The greatest changes occur in the equatorial Western Pacific and the South Pacific convergence zone, where there is a pronounced decrease in precipitation, suggesting that longwave atmospheric CRF forces precipitation in these regions. Weaker but spatially coherent decreases also occur in the winter midlatitudes. These

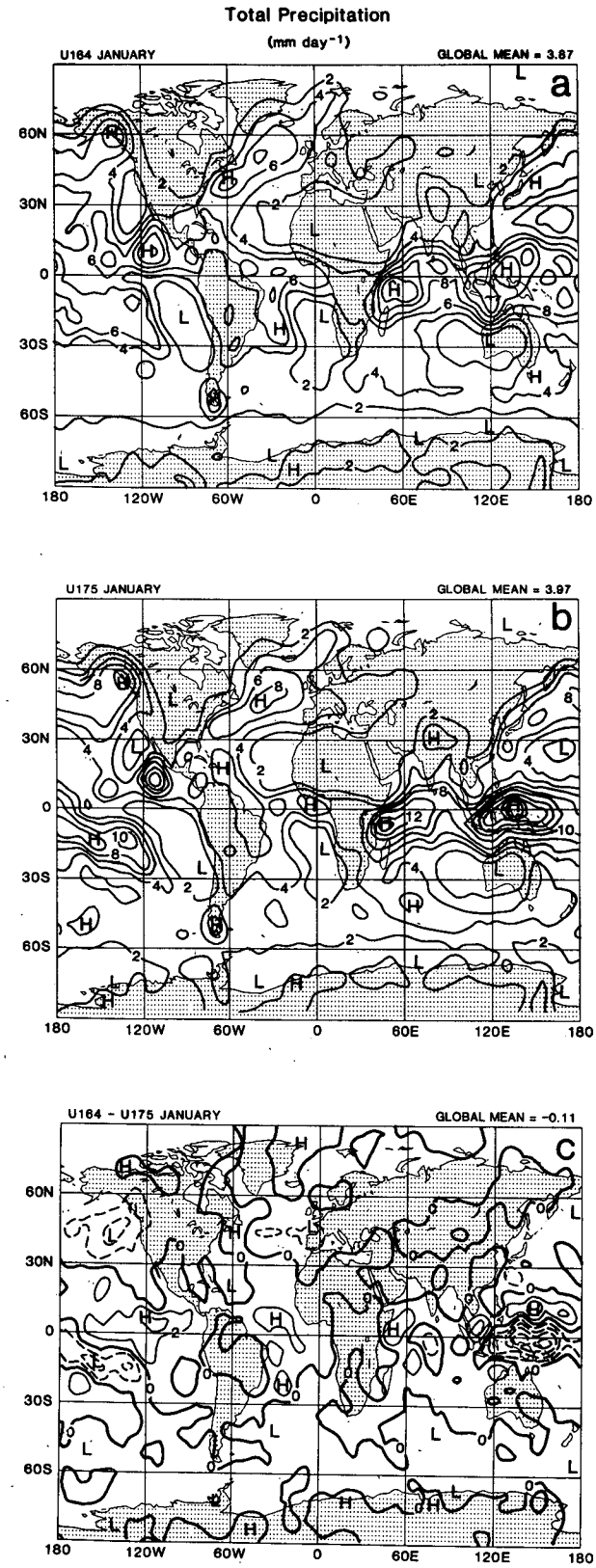

FIG. 15. Total precipitation for (a) the NOCRF experiment, (b) the control, and (c) the difference.

results are consistent with those of S^2 (their Fig. 11), who concluded that the effect of the cloud longwave forcing in the CCM is to enhance the moist convection in areas where it is already strong. On the other hand, in the UCLA/GLA GCM, the ACRF actually causes the precipitation to *decrease* substantially in the *eastern* Equatorial Pacific and the Atlantic ITCZ; regions of decrease can also be found in the results of S^2. Further discussion of these ambiguities is given in the next section.

The level of MSTADJ activity decreased by about 10% in the experiment, suggesting that radiative forcing plays only a minor role in driving it.

Figure 16a shows the zonally averaged difference in temperature between the NOCRF experiment and the control. In both GCMs, the changes in the tropical temperatures correspond very simply to the changes in the longwave cooling. We find that the ACRF leads to a cooling of the tropical upper troposphere, by several degrees, while S^2 actually obtain a warming of about the same magnitude. In both the CCM and the UCLA/GLA model, the ACRF leads to warming of several degrees in the tropical middle troposphere Figures 16b and c show that in the UCLA/GLA GCM the ACRF acts to increase both the relative humidity and the mixing ratio of water vapor at low levels in the tropics; in fact, it increases the precipitable water content of the tropical atmosphere by several percent. In contrast, S^2 found a small increase in the specific humidity at 800 mb, but little change at lower levels and little change in the precipitable water. In the UCLA/GLA GCM, the ACRF actually causes the relative humidity to decrease in the tropical middle troposphere. This is due to the warmer temperatures there, and also to the increased drying associated with stronger deep convection. Figure 16d shows that the ACRF leads to an increase in the low-level cloudiness at all latitudes, while middle-level cloudiness decreases in the tropics, roughly where the temperature increases and the relative humidity decreases. PBL stratocumulus cloudiness increases in response to the ACRF, especially over the ocean around Antarctica.

Slingo and Slingo found a strong wavelike pattern in the 200 mb height difference between their experiment and their control. Although the UCLA/GLA GCM also responds strongly (Fig. 17), the two models differ significantly in the positions and intensities of their height anomalies. This is not surprising, since their perturbation heating fields are also quite different.

4. Seaworld

As noted above, although the NOCRF experiments performed with the CCM and the UCLA/GLA GCM both suggest that the ACRF acts to increase the precipitation rate over the tropical oceans, there are some regions in which the precipitation rate actually de-

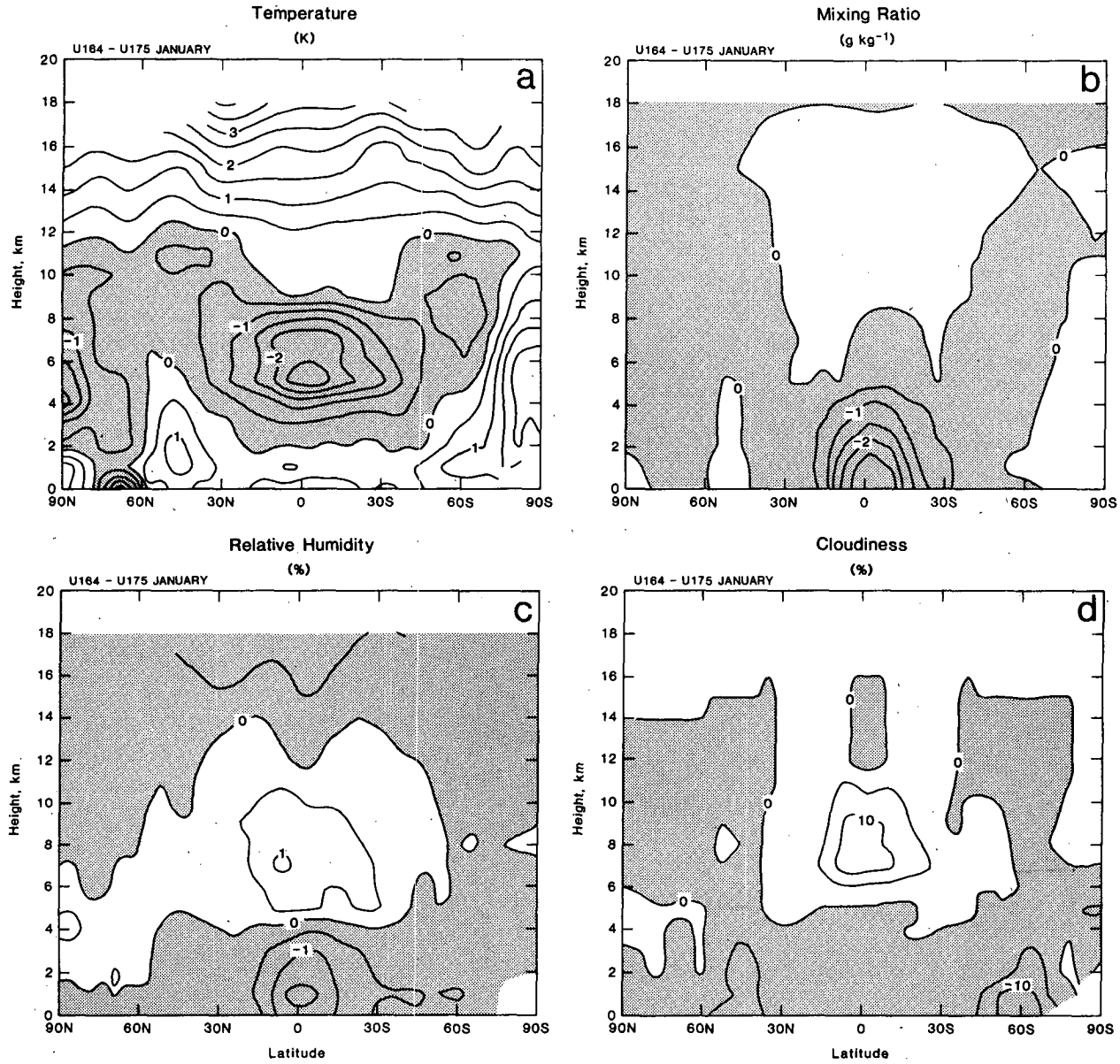

FIG. 16. Zonally averaged change between the NOCRF experiment and the control, for (a) temperature, (b) mixing ratio, (c) relative humidity, (d) cloudiness.

creases. We hypothesize that the Earth's complex land–sea geometry is responsible for this puzzling situation.

To test this hypothesis, we decided to simplify the problem by performing simulations with an ocean-covered Earth, which we call "Seaworld." The sea-surface temperatures of Seaworld are prescribed and zonally uniform, as shown in Fig. 18, and are based on the simulated zonally averaged (including both land and sea) boundary temperature obtained in the July simulation discussed earlier. A perpetual July is assumed. For simplicity, an albedo appropriate to the oceans is used everywhere; we have not included any effects of sea ice. The key simplifications of Seaworld are the fixed boundary temperatures with no land points, the lack of mountains, and the zonal uniformity of the boundary conditions. An ocean-covered planet similar to Seaworld was used by Hayashi and Sumi (1986) to investigate the 30–40 day oscillation. Because of its relative simplicity, we believe that studies of Seaworld can be useful to develop better understanding of the basic dynamics of the atmospheric general circulation. As Lorenz (1967) pointed out, "Within the collection of possible planetary atmospheres, one which is devoid of irregularities occupies a more central and fundamental position than one with any specific arrangement of irregularities."

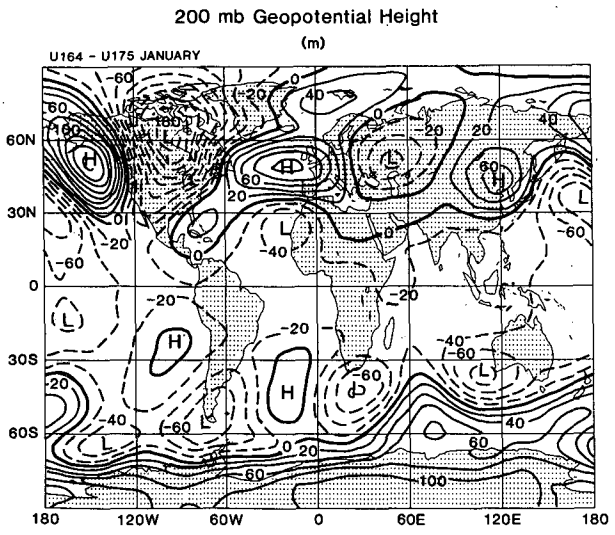

FIG. 17. Change in 200 mb height between the NOCRF experiment and the control. The contour interval is 20 m, the zero contour is heavy, and negative contours are dashed.

Our Seaworld simulations were initialized from the 1 June conditions of the June–July Earth simulation. All boundary conditions were instantaneously changed to those of Seaworld, except that the mountains were gradually flattened out over a duration of two simulated days, to avoid extreme sloshing of the model atmosphere. We performed two 90-day Seaworld simulations, and analyzed the last 60 days of each. The first included all of the model's physical parameterizations, while the second omitted the effects of clouds in both the solar and terrestrial radiation parameterizations. Since the boundary temperatures are fixed and identical in the two runs, the clouds can affect the results *only* through the ACRF; the differences between the two runs, therefore, reveal the direct and indirect effects of the ACRF.

Figure 19 shows the latitude–height distribution of the total (solar plus terrestrial) ACRF in the run with clouds, as well as the latitude–height distribution of the difference in the zonally averaged total radiative heating between the two runs. Except at low levels in the tropics, there is a very strong quantitative similarity between the two figures, indicating that, for the most part, the ACRF in the cloudy run accurately represents the radiative heating perturbation relative to the cloud-free fun. Figure 20 shows the integral of the ACRF across the atmosphere in the cloudy run. This represents a warming of up to 70 W m^{-2} in the Northern Hemisphere tropics. Also shown in Fig. 20 are the *change* in the net radiation into the atmosphere (including both the Earth's surface and the top of the atmosphere), and the *change* in the total energy flux into the atmosphere, from both radiation and turbulent sensible and latent heat fluxes. The change in the net radiation between the two runs essentially reflects the existence of ACRF in the cloudy run, but is less positive. The change in the total energy flux is similar to the change in the ACRF, but the tropical peak is higher. Apparently, the tropical atmosphere adjusts to the ACRF in such a way that *the energy input due to the ACRF is amplified, i.e., there is a positive feedback.*

Figure 21 shows the zonally averaged 200 mb height and precipitable water for both runs. The 200 mb surface is significantly higher in the tropics when clouds are present, because high clouds warm the tropical troposphere by trapping outgoing longwave radiation. Interestingly, the clouds act to drastically increase the moisture content of the atmosphere. The cloudy run has much more precipitable water than the cloud-free run—almost twice as much in the tropics. The atmospheric moisture content of the cloudy Seaworld is much more Earth-like than that of the cloud-free Seaworld, although of course it is not clear to what extent we should expect Seaworld to resemble Earth. The simulated temperature and moisture differences between the two runs are shown in more detail in Fig. 22, which gives the latitude–height sections of the temperature and specific humidity differences. As would be expected from Fig. 19, the ACRF warms the middle troposphere at the 6 km level; this warming reaches 8°K. Not surprisingly, the specific humidity increase in the cloudy run is confined to the lower troposphere, where the saturation specific humidity is relatively large. The increased precipitable water content of the cloudy model atmosphere cannot be explained by assuming fixed relative humidity and taking into account the warmer temperatures, because the warming in the cloudy run occurs primarily in the middle troposphere where the specific humidities are necessarily small. Near the surface, where the specific humidities are relatively large, the temperature does not differ much between the two runs, since the same fixed boundary

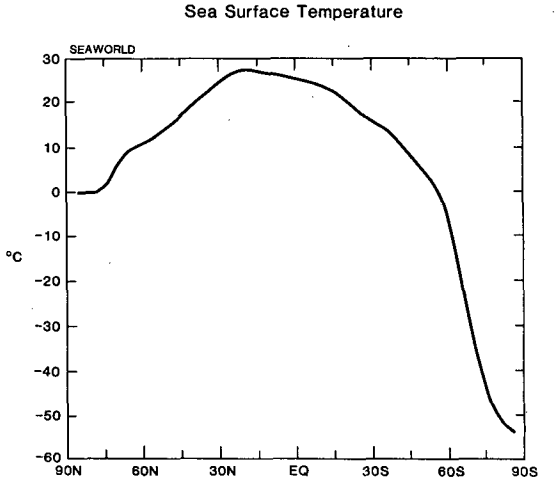

FIG. 18. Meridional distribution of the zonally uniform sea surface temperature used in both Seaworld simulations.

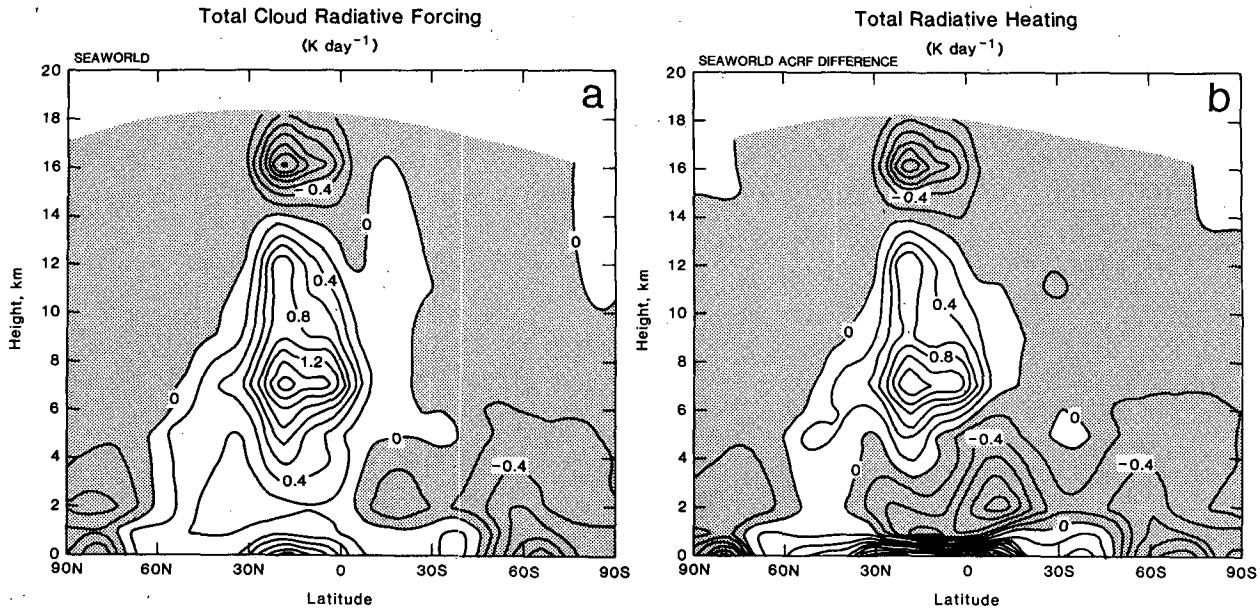

FIG. 19. Latitude–height distributions of (a) the zonally averaged total ACRF in the Seaworld run with clouds and (b) the difference between the zonally averaged total radiative heating in the cloudy Seaworld run and that in the cloud-free run.

temperatures were used in both. The actual reason for the increased moisture content of the cloudy atmosphere involves the large-scale motions, as discussed further below.

Referring back to Figs. 19 and 20, it is clear that the change in the net radiation is less than the change in the ACRF, mainly because of the increased water vapor in the tropical lower troposphere, which leads to stronger infrared cooling at low levels.

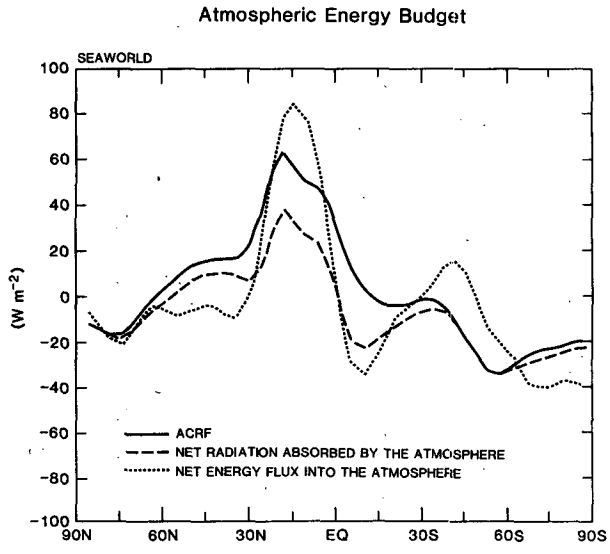

FIG. 20. Differences between the Seaworld simulations with and without clouds. Solid line: The integral of the ACRF across the atmosphere. Dashed line: Net radiation into the atmosphere, including both the Earth's surface and the top of the atmosphere. Dotted line: Total energy flux into the atmosphere, from both radiation and turbulent sensible and latent heat fluxes.

Figure 23 shows the zonally averaged precipitation, evaporation, and the difference, for both the clear and cloudy runs. The globally averaged precipitation and evaporation are about 15% greater in the cloudy run, which is a remarkably small change considering the large difference in the moisture content of the atmosphere. The additional latent heating associated with the increased rate of precipitation is required to balance the stronger radiative cooling that occurs in the cloud-free atmosphere. There is a double tropical rain band in the cloud-free run, and a single, more intense tropical rain band in the cloudy run. Generally, the precipitation is much more concentrated in the cloudy run. Tropical evaporation increases significantly in the cloudy run. Of course, this increased evaporation is necessary to balance the more rapid drying of the atmosphere by convection. It is partly due to the fact that the tropical PBL air is about 2 g kg^{-1} drier in the cloudy run, and partly due to a 3 m s^{-1} increase in the PBL wind speed in the cloudy run. Krishnamurti et al. (1988) have emphasized the importance of surface wind speed fluctuations for producing latent heat flux changes over the Earth's tropical oceans. The increased surface latent heat flux in the cloudy run accounts for the "amplification" of the atmospheric energy source due to the ACRF, as seen in Fig. 20.

Figure 24 shows that the cloudy run produces convection about 30% of the time in the tropics, while the cloud-free run produces almost incessant convection. Recall from Fig. 23 that the tropical precipitation rates are comparable in the two runs. It thus appears that

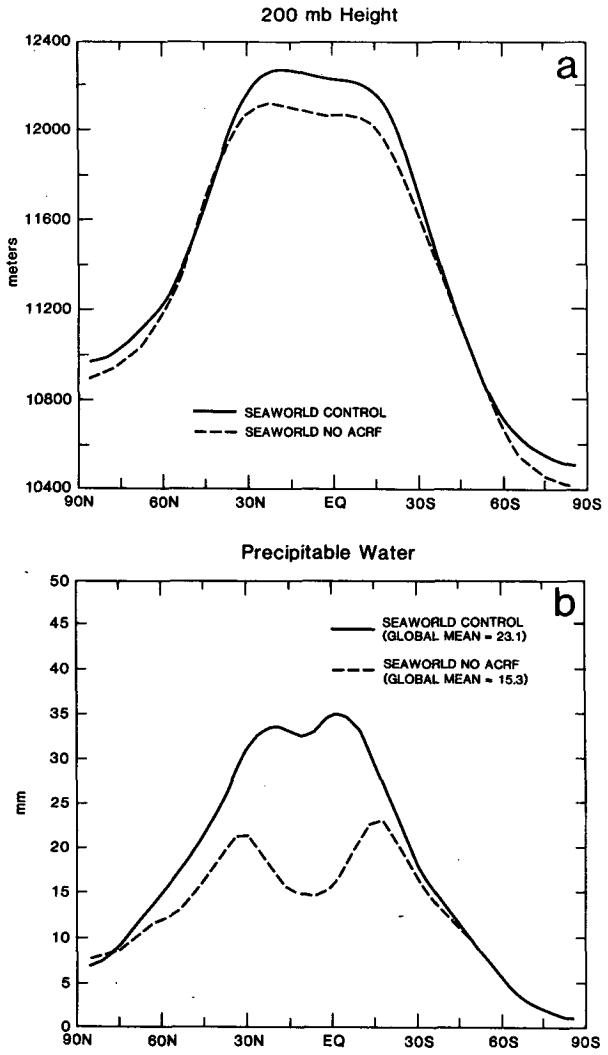

FIG. 21. Zonal averages of (a) 200 mb height and (b) precipitable water for both Seaworld simulations. The solid line shows the cloudy run, and the dashed line shows the cloud-free fun.

ACRF favors more intense but less frequent convection. Without radiatively active clouds, the tropical troposphere is radiatively destabilized at an almost constant rate, and this steady radiative destabilization is balanced by steady but weak convection. When radiatively active upper-level clouds are permitted to form, they interrupt the tropospheric cooling and so tend to cut off the convection that gave rise to them. The system is then subject to spasmodic convection, which is less frequent but more intense.

In view of the results presented above, it will come as no surprise that the mean meridional circulation differs quite substantially between the two simulations. As shown in Fig. 25, both runs produce two Hadley cells—a weak cell in the Northern Hemisphere and a strong one straddling the equator. With clouds, the main Hadley cell transports about 240×10^9 kg s^{-1}, and is centered on the equator, with its rising branch at about 10°N. Without clouds, it transports only about 120×10^9 kg s^{-1}, and is centered at about 10°S. In both simulations, the stronger cell transports about 6 times as much mass as the weaker cell. The cloud-free simulation produces a relative minimum of the zonally averaged rising motion near 10°N, where the simulated precipitation also has a minimum (cf. Fig. 23). The relatively strong rising branches both north and south of this minimum are associated with the two precipitation maxima shown in Fig. 23, and with the latent heating maxima discussed below. The mean meridional

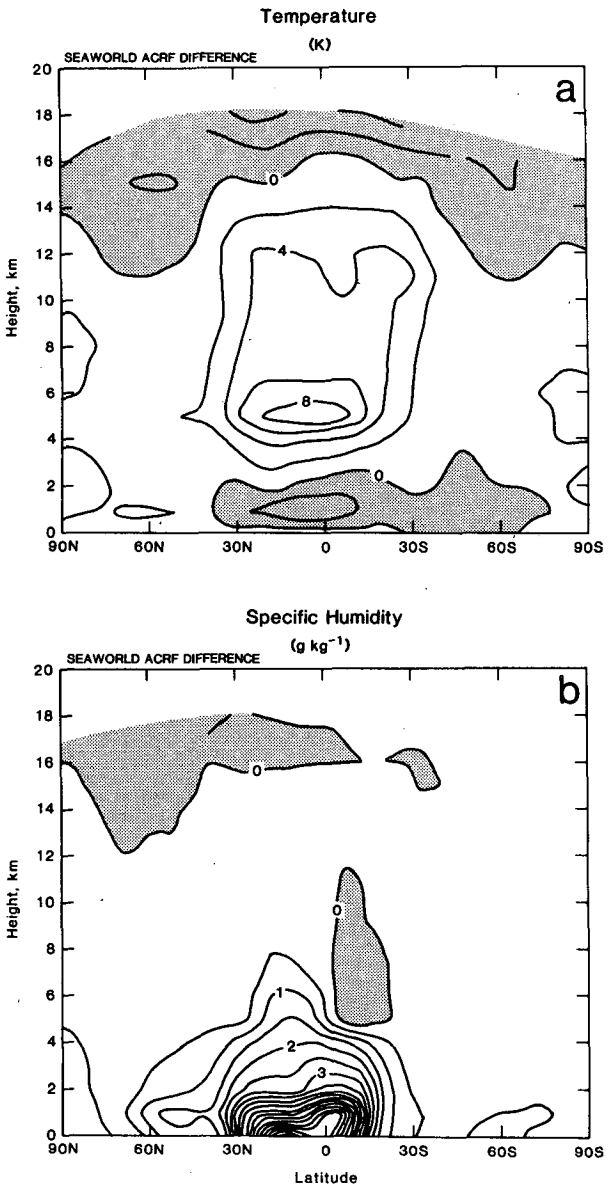

FIG. 22. Latitude–height sections of the differences (cloudy minus cloud-free) for (a) temperature and (b) specific humidity between the two Seaworld simulations.

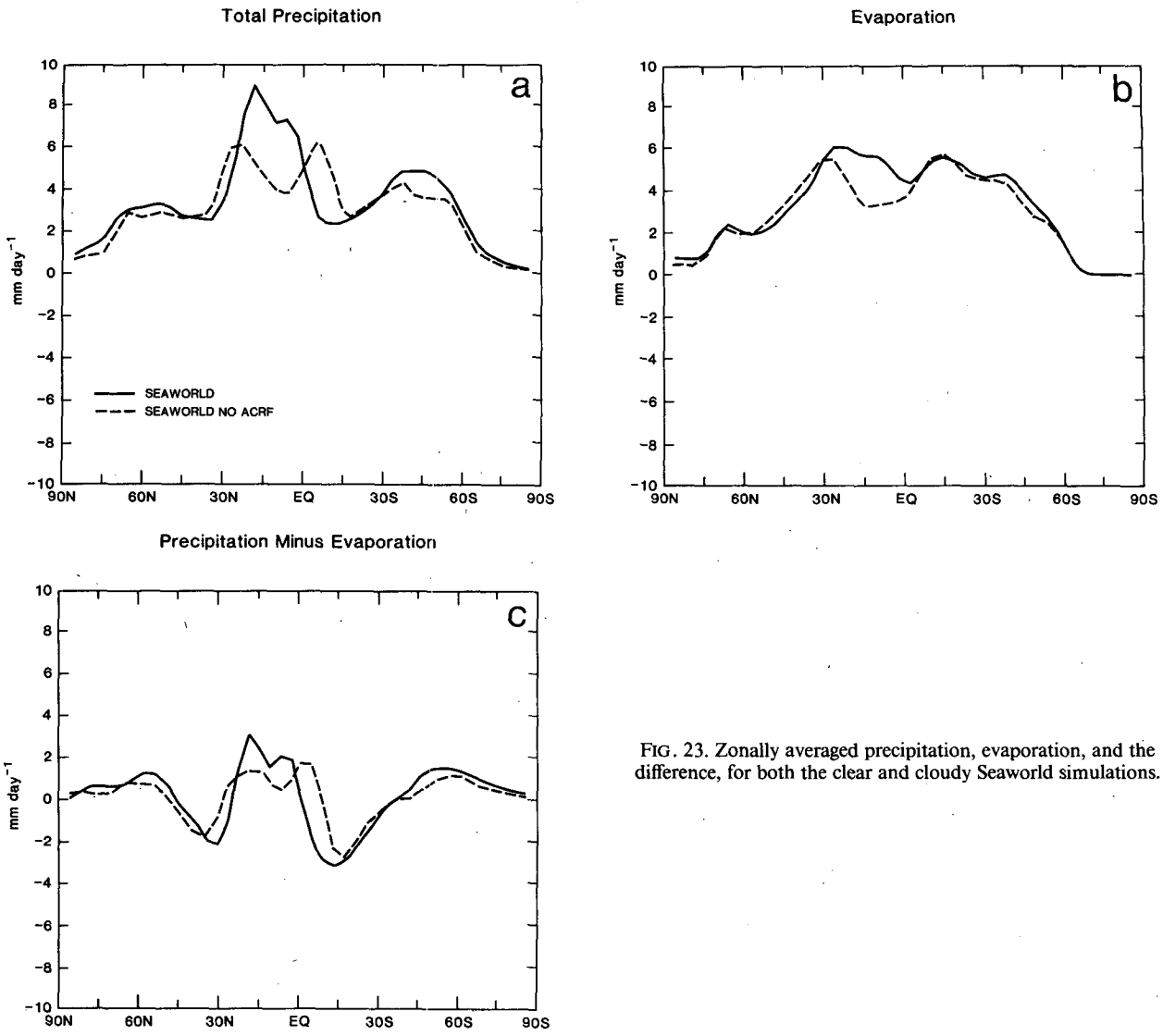

FIG. 23. Zonally averaged precipitation, evaporation, and the difference, for both the clear and cloudy Seaworld simulations.

circulation of the cloudy simulation is considerably more Earth-like than that of the cloud-free simulation.

The stronger Hadley circulation in the cloudy run accounts for the increased tropical PBL wind speed that leads to the stronger surface evaporation discussed above. This is a critical link in the positive feedback loop that amplifies the heating produced by the ACRF.

The latitude–height distributions of cumulus heating and total latent heating are shown in Figs. 26 and 27, respectively. When ACRF is present, the system selects a relatively narrow but intense zone of latent heating near 15°N, coinciding with the rising branch of the Hadley cell shown in Fig. 25. The cloud-free run has two relatively weak convective heating maxima, near 10°S and 25°N.

Naturally, the zonal wind is strongly influenced by the changes discussed above. Figure 28 shows the zonally averaged zonal wind in the cloudy run, as well as the difference between the cloudy run and the cloud-free run. The ACRF increases the intensity of the tropical easterlies, particularly near the surface and the tropopause; and it also enhances the subtropical westerly jets, shifting them equatorward. Ramanathan et al. (1983) also found considerable sensitivity of the zonally averaged zonal wind to the distribution and optical properties of the clouds.

The PBL is considerably deeper in the cloudy run. This is particularly noticeable near 10°N, where the cloudy run has strong low-level rising motion. Increased large-scale convergence favors an increased PBL depth in this region. A deeper PBL is also favored by the warmer troposphere in the cloudy run, which implies a weaker inversion at the PBL top; and by radiative cooling at the tops of PBL stratus clouds, which promotes rapid entrainment.

As a result of the increased PBL depth, the precip-

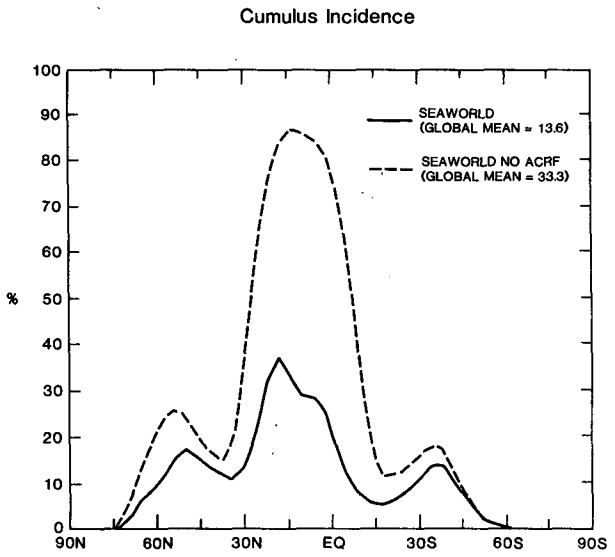

FIG. 24. Zonally averaged frequency of cumulus convection, for both the clear and cloudy Seaworld simulations.

itable water content of the PBL is much larger in the cloudy run, even though, as noted above, the PBL specific humidity is actually slightly smaller. Most of the simulated increase in the precipitable water occurs in the troposphere above the PBL, however. As discussed in section 2, cumulus detrainment is the most important mechanism for supplying the increased moisture to the free atmosphere. The moisture is then redistributed vertically, through advection by the rising branch of the Hadley cell, and also by large-scale precipitation/reevaporation.

Figure 29 shows the cumulus detrainment intensities for the two runs, as a function of latitude and height. This plot essentially shows where the cumulus clouds have their tops. The units are inverse days; the timescale is that for replacement of all of the air in a unit volume by new air detrained from cumulus towers (Arakawa and Schubert 1974). The cloudy run has a prominent maximum of detrainment precisely where Fig. 19 shows intense negative cloud forcing due to cumulus anvil tops. This suggests that the intense deep convection in the ITCZ of the cloudy run is promoted by radiative destabilization of the column. Of course, it is also favored by the increased strength of the Hadley circulation, which, in turn, is invigorated by the greater warming at 10°N, due to both ACRF and cumulus convection.

Finally, Fig. 30 shows the cloudiness distributions for both runs. Of course, in the "cloud-free" run the clouds were radiatively inactive, but nevertheless we saved their distribution as a diagnostic. The upper tropical troposphere is almost twice as cloudy in the "cloud-free" run as in the cloudy run. This is due to the increased frequency of cumulus activity, which leads to greater anvil cloudiness, associated with cooler temperatures, but it is also partly due to an increase in the relative humidity there.

The ACRF is the only difference between the model formulations used in the two Seaworld runs. Its effects on the radiative-convective-dynamical system of Seaworld are dramatic, to say the least. It locally intensifies deep cumulus convection, reduces the cumulus incidence, amplifies the mean meridional circulation, and dramatically increases the moisture content of the atmosphere, at the same time reducing the upper level cloudiness that is primarily responsible for the ACRF. All of this occurs with only minor changes in the *globally averaged* precipitation or evaporation rates. These results are qualitatively consistent with but quantitatively much stronger than those of the CCM-based ex-

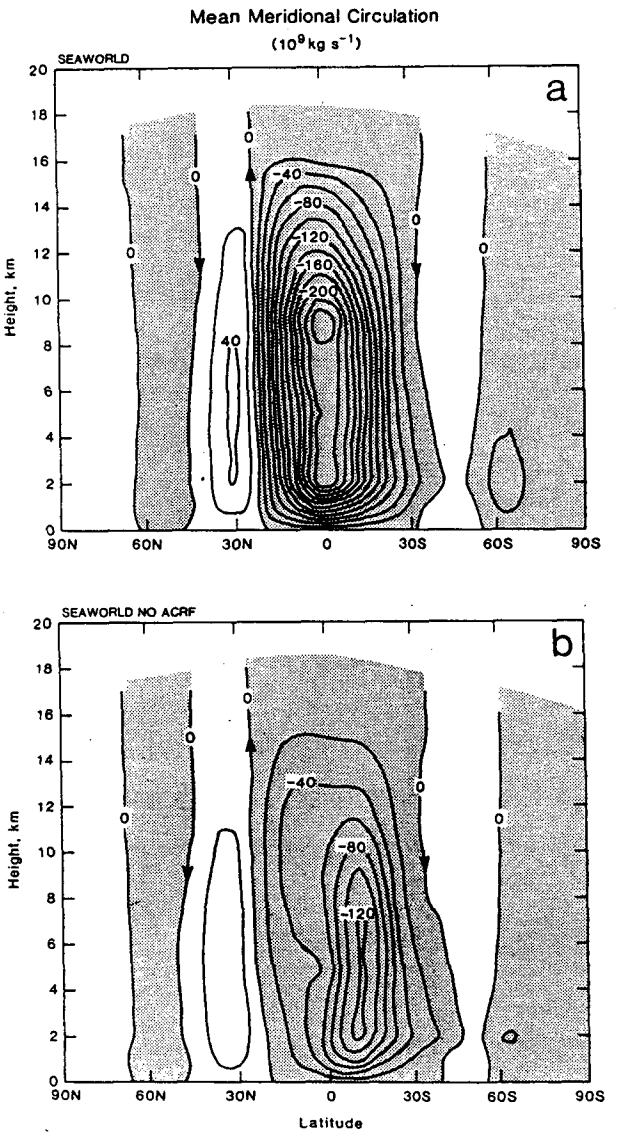

FIG. 25. Mean meridional circulations for both Seaworld simulations.

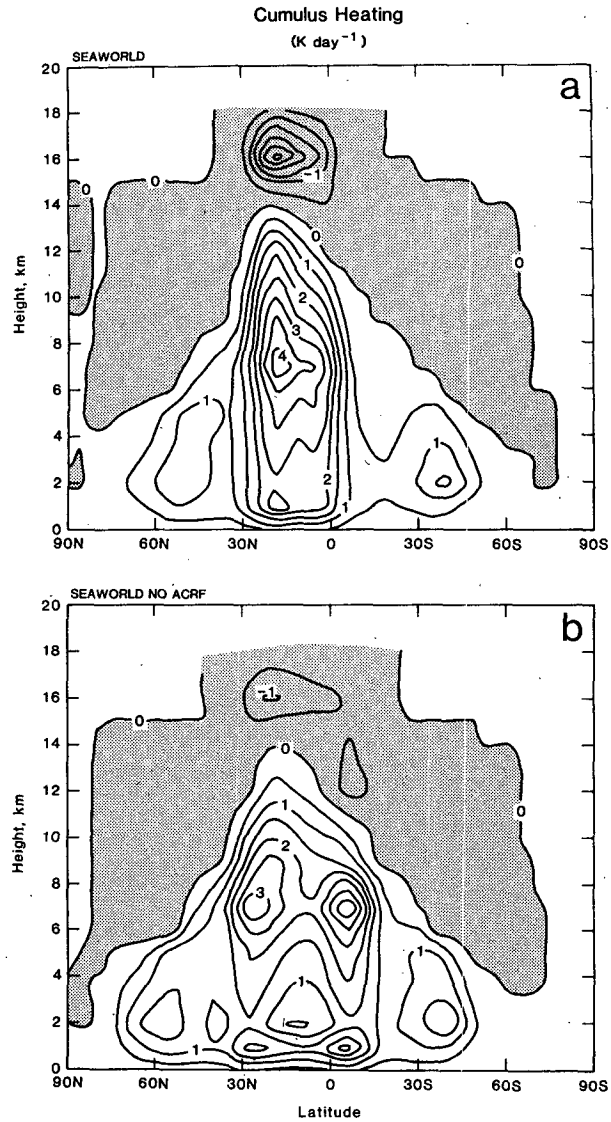

FIG. 26. Latitude–height sections of cumulus heating for the cloudy and cloud-free Seaworld simulations.

periment of Slingo and Slingo (1988), who found that the effect of the ACRF is to "enhance the total precipitation and vertical velocity in areas where these are already large;" they are also consistent with the results of the NOACRF experiment described in the preceding section. We believe that the much stronger response in the Seaworld simulation stems from the absence of continents. It appears therefore, that the effects of the ACRF differ greatly over continents and oceans.

How does the ACRF produce its effects on the climate of Seaworld? The key to this puzzle is the apparent tendency of the ACRF to promote deep cumulus convection. The results presented above suggest two possible mechanisms for this. First, as shown by HRCD, the ACRF associated with deep convection produces a net warming of the vertical column, relative to neighboring columns where convection is not active. This warming tends to promote large-scale rising motion in the convective region, and so tends to accelerate the rising branch of the Hadley circulation. The stronger rising motion then favors an intensification of the convection. The second possible mechanism involves the vertical distribution of the ACRF, which is shown in Fig. 19. When ACRF is included, radiative cooling at the tops of anvils destabilizes the column with respect to deep penetrative convection from the PBL, as well as moist adjustment in the upper tropical troposphere. The increased latent heating, together with the vertically averaged radiative heating, can then drive an intensified mean meridional circulation. Either or both

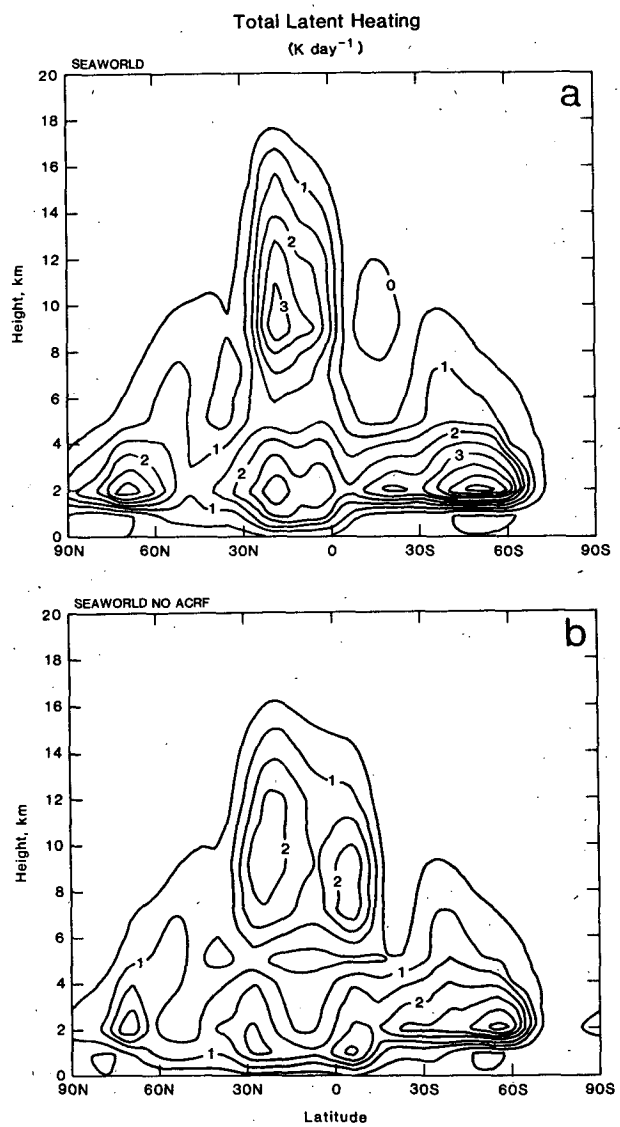

FIG. 27. Latitude–height sections of total latent heating for the cloudy and cloud-free Seaworld simulations.

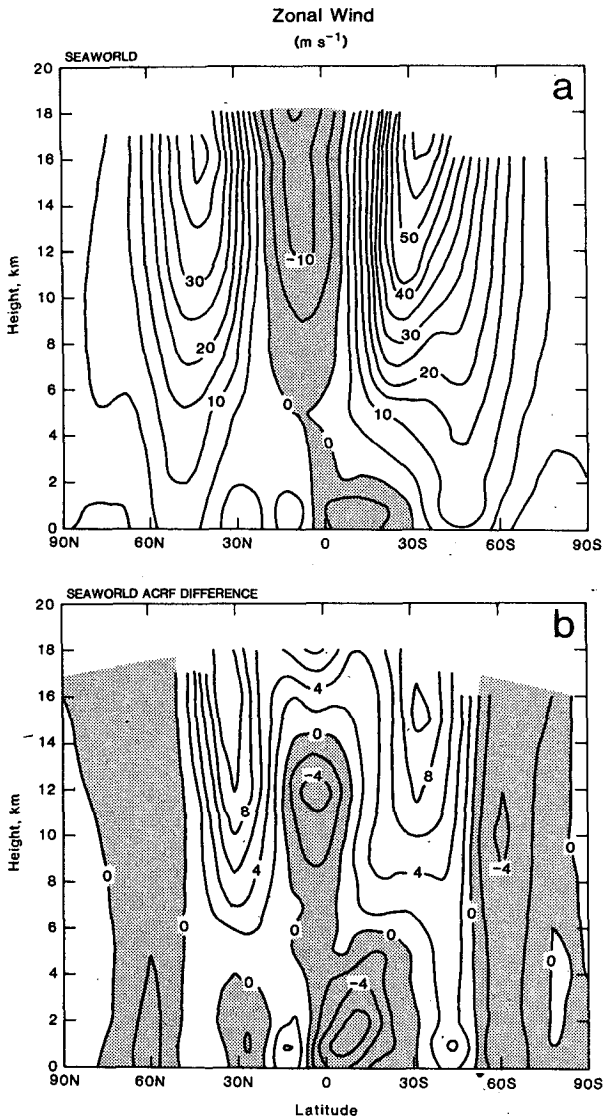

FIG. 28. The zonally averaged zonal wind in the cloudy run, as well as the difference in the zonally averaged zonal wind between the cloudy run and the cloud-free run.

of these two mechanisms could act to intensify convection.

To explore their relative importance, we performed a further experiment in which we computed the ACRF in the usual way, but vertically averaged it before adding it into the temperature tendency. The results of this experiment closely resemble those of the cloudy Seaworld run discussed above, showing that it is the vertical mean of the ACRF rather than its vertical distribution that gives rise to the various effects described above. This implies that the intensified cumulus convection of the cloudy run is forced by the stronger large-scale rising motion, rather than directly by radiative effects. Nevertheless, we cannot rule out the possibility that the vertical distribution of the ACRF has significant effects on the large-scale circulation and moist convection.

The dominance of the vertical mean of the ACRF, rather than its vertical structure, helps to explain the general agreement between the results of the NOCRF experiments performed with the CCM and the UCLA/GLA GCM, in spite of the great differences in the vertical profiles of the ACRF produced by the two models.

We speculate that the Northern Hemisphere Hadley circulation is selectively amplified by the ACRF because the sea surface temperatures are warmer there. The subsidence associated with the strong Northern Hemisphere Hadley cell tends to suppress the Southern

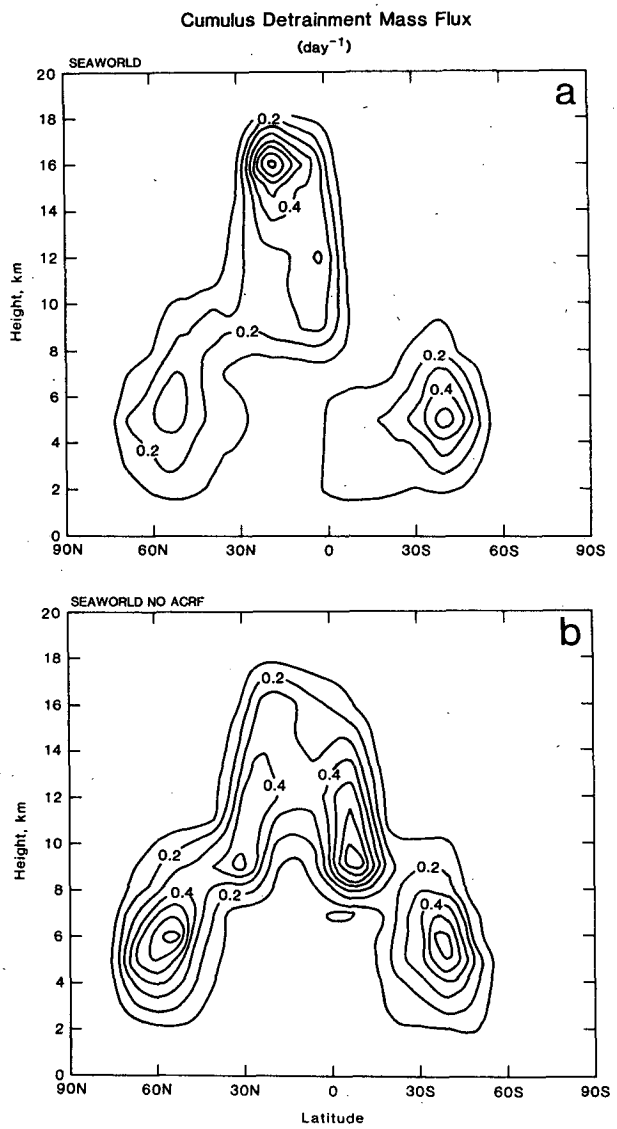

FIG. 29. The zonally averaged cumulus detrainment intensities for the cloudy and cloud-free Seaworld simulations. The units are inverse days. The time scale represents how long it would take cumulus clouds to replace the ambient air by newly detrained air.

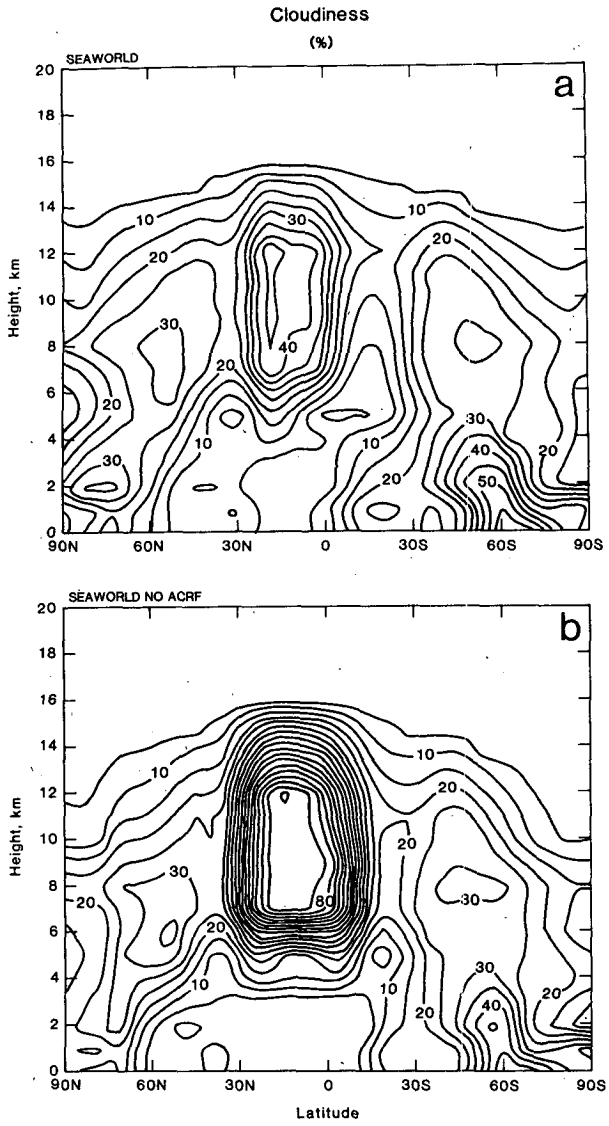

FIG. 30. The latitude–height distribution of the zonally averaged cloudiness for the cloudy and cloud-free Seaworld simulations.

Hemisphere Hadley cell and its associated precipitation.

Our results illustrate a three-way interaction among the ACRF, the convection, and the large-scale dynamics. The feedbacks among the three components are strongly positive. At the same time, however, each of the three components feeds back negatively on itself: the ACRF tends to reduce the cloudiness by reducing the cumulus incidence and the relative humidity; the convection increases the moist static stability of the column and so tends to shut itself off; and the large-scale circulation depletes its own source of available potential energy. These negative feedbacks determine how the system equilibrates.

The present analysis has not explained why the cloud-free run produced a double tropical rain band, while the cloudy run produced a single rain band. This question merits further study.

5. Summary and conclusions

The main subjects of this paper are the net effects of the CRF on the atmospheric general circulation and the mechanisms through which these effects are produced, with emphasis on the effects of high clouds and especially cumulonimbus anvils. Our results reveal the highly interactive nature of the cloud/radiation problem. Cloudiness modifies the radiation field, but at the same time radiative effects play an important role in the *generation* of the model clouds; both convection and the large-scale circulation act as intermediaries in this process. Wetherald and Manabe (1988) have also pointed out the importance of interactions between radiatively active cloudiness and convection. Some of these cloud–radiation interactions occur on time and space scales too small to be explicitly resolved by the GCM, so that the interactions themselves must be parameterized, implying that we can no longer justify *independent* development of these parameterizations.

One deficiency of our Earth simulations is that the simulated convective precipitation maxima tend to be more intense than observed. For the oceans, this may indicate excessive sensitivity to the ACRF, perhaps due to our lack of a fractional cloudiness parameterization. The simulated evaporation and precipitation are both considerably stronger than observed over the Northern Hemisphere continents in summer, suggesting the need to parameterize the effects of vegetation, and perhaps indicating that too much radiation reaches the ground in these regions. Shallow convection tends to be underpredicted by the GCM, perhaps in part because its radiative effects have been neglected, and in part because the model's vertical resolution is inadequate. Various deficiencies of our results suggest that every single term of the model's moisture conservation equation needs work. We strongly suspect that the same is true of other GCMs.

We have performed numerical experiments to uncover particular interactions among the parameterized processes of the GCM. In the NODETLQ experiment, we perturbed the model's water vapor budget, by eliminating the detrainment of cloud particles from deep cumulus clouds. The simulated upper-level cloudiness proved to be quite sensitive to this change. Neither the CONTROL nor the NODETLQ experiment realistically represents the complex processes of cumulus detrainment and anvil precipitation, however.

In the NOANVIL experiment, we perturbed the model's cloud formation algorithm, by omitting the radiative effects of cumulus anvils. Surface evaporation

accelerated, the precipitable water increased, and deep convection intensified. The surface and the atmosphere both warmed, even though the change in the *atmospheric* CRF would, by itself, tend to cool the atmosphere. These results demonstrate that the surface solar CRF is very important, even in a model with fixed sea surface temperatures. They also show that cumulus anvil clouds, as parameterized in the model, exert a very powerful influence on deep tropical convection by tending to radiatively destabilize the troposphere. In addition, of course, the anvils radiatively warm the column in which they reside, by trapping terrestrial radiation. Although the simulated effects of these clouds are qualitatively consistent with the observations of Houze (1977) and Ackerman et al. (1988), their strong influence on the simulated climate argues for a much more refined parameterization.

The NODETLQ and NOANVIL experiments taken together show that, in the present model, both anvils and moistening by detrained condensate are needed to maximize the realism of the radiation budget at the top of the atmosphere. A more realistic anvil parameterization might be based on a prognostic cloud water (or ice) variable, for which cumulus detrainment would represent an important source term.

In the NOCRF experiment, the longwave ACRF was omitted, as in the CCM study by Slingo and Slingo (1988). Our results are generally consistent with theirs, and represent further evidence that the atmospheric longwave CRF acts to enhance precipitation, particularly in the tropics, mainly by spatially concentrating the precipitation without drastically increasing the total over the globe. These effects are primarily due to the anvil clouds.

Our Seaworld results provide additional strong support for this conclusion, and suggest that the ACRF has a powerful influence on such basic climate parameters as the strength of the Hadley circulation, the existence of a single narrow ITCZ, and the precipitable water content of the atmosphere. This conclusion must be viewed with caution, however. Our "Earth" simulations show that clouds tend to cool the tropical oceans and land surface, and to warm the tropical atmosphere. This indicates that, when the effects of clouds on the land surface and sea surface are taken into account, the CRF may feed back negatively to suppress moist convection and the associated cloudiness.

The NOCRF and Seaworld experiments taken together strongly suggest that the atmospheric CRF and the surface CRF have strongly opposing effects on convection and the hydrologic cycle: the atmospheric CRF accelerates them, while the surface CRF brakes them. In addition, over the oceans the surface CRF acts on a much longer time scale than the atmospheric CRF. For these reasons, it is important to realistically simulate *both* the atmospheric and surface components of the CRF; realistic simulation of the total CRF acting on the earth–atmosphere system is not sufficient for successful climate simulation.

Many current climate models, including ours, have fixed sea surface temperatures but variable land-surface temperatures. Our results imply that the mean meridional circulations of such models experience a positive feedback due to ACRF over the oceans, and a negative or weak feedback over the land. Unfortunately, it will be difficult to address such issues observationally, because the surface energy balance is particularly difficult to observe. The effects of the CRF on the climate system can only be firmly established through much further analysis, which can benefit greatly from the use of a coupled ocean–atmosphere model.

Each of our experiments produced major changes in the simulated radiation, cloudiness, and/or hydrologic cycle. These aspects of the model's climate are evidently very sensitive to what might be considered "details" of the formulation, suggesting that they can be tuned, either deliberately or accidentally, to agree with observations. Such tuning may be justified for numerical weather prediction, but it defeats the purpose of climate simulation studies, which are intended to reveal the processes that tend to maintain the climate and/or regulate climate change.

The common conclusion of all of the experiments is that *the upper tropospheric cloudiness associated with cumulus convection has a powerful influence on both the convection and the large-scale circulation.* Unfortunately, existing general circulation models do not include adequate parameterizations of upper-tropospheric clouds or the convective processes that give rise to them. The diverse effects of moist convection are still parameterized crudely in all existing models. For example, the obvious physical links between latent heating and moist convection on the one hand, and the radiative properties of the clouds on the other, are not consistently accounted for. "Large-scale saturation" parameterizations are used to represent the stratiform precipitation, which is typically assumed to fall out instantaneously, despite observational evidence that ice crystals, in particular, can have long lifetimes. *No existing GCM includes a direct, physically consistent representation of the radiative, thermodynamical, and dynamical couplings between the convection parameterization and the large-scale saturation parameterization, despite the overwhelming observational evidence* (e.g., Houze 1977, 1982; Webster and Stephens 1980; Rutlege and Houze 1987; Heymsfield and Miller 1988) *that such couplings exist.* Future model development efforts must address these complex and interesting issues.

Acknowledgments. Prof. S. Cox and Dr. J. Coakley, Jr. provided strong encouragement for completion of this study. Dr. A. Slingo helped us to understand the

CCM results. This research has been supported by NASA's Climate Program, in part through Grant NAG 5-1058. Computing resources were obtained through the Numerical Aerodynamic Simulation Facility at NASA/Ames.

APPENDIX

A Brief Description of the UCLA/GLA General Circulation Model

The UCLA/GLA GCM has been derived from the UCLA GCM, which was developed at UCLA, over a period of 20 years, by A. Arakawa and collaborators. A copy of the model was brought to GLA in 1982. Many changes have been made at GLA; the most important of these are revised solar and terrestrial radiation parameterizations (Harshvardhan et al. 1987).

The prognostic variables of the current UCLA/GLA GCM are: potential temperature, the mixing ratios of water vapor and ozone, the horizontal wind components, the surface pressure, the planetary boundary layer's depth and turbulence kinetic energy, the ground temperature and snow depth at land points, and the ice temperature at land ice and sea ice points. The governing equations are finite-differenced, using highly conservative schemes. Fourier filtering of the mass flux and pressure gradient vectors is used to maintain computational stability near the poles. The model has been programmed so that the hoizontal and vertical resolutions and the pressure of the model top are easily varied. The code is portable enough to run on a variety of computers.

A key feature of the GCM is its formulation in terms of a modified sigma coordinate, in which the planetary boundary layer (PBL) top is a coordinate surface, and the PBL itself is the lowest model layer. As already mentioned, the PBL depth is a prognostic variable of the model. The turbulence kinetic energy of the PBL has recently been introduced as a prognostic variable, following Randall et al. (1988). The mass sources and sinks for the PBL consist of large-scale convergence or divergence, turbulent entrainment, and the cumulus mass flux. Turbulent entrainment can be driven by positive buoyancy.

The cumulus mass flux and the warming and drying of the free atmosphere due to cumulus convection are determined through the cumulus parameterization of Arakawa and Schubert (1974). The ice phase is taken into account in the cumulus parameterization, but not in the large-scale saturation parameterization. Rain falling through unsaturated grid boxes is allowed to evaporate if it originates through large-scale saturation at an upper level, but not if it originates in cumulus towers. Cumulus friction is included. The implementation of the Arakawa-Schubert scheme generally follows the description of Lord et al. (1982), except that we do allow detrainment of cloud liquid and ice from all cumulus clouds (see the discussion of HRCD).

The Arakawa–Schubert parameterization currently applies only to clouds that draw their mass from the PBL. There are, of course, moist convective motions that originate above the PBL. These are parameterized through a conventional convective adjustment.

The radiation parameterization of the model has recently been revised by Harshvardhan et al. (1987). The terrestrial radiation parameterization includes cooling due to water vapor, carbon dioxide, and ozone. The solar radiation parameterization includes Rayleigh scattering and absorption by water vapor and ozone, and simulates both the diurnal and seasonal cycles. A complete (solar and terrestrial) radiation calculation is done once per simulated hour, in order to resolve adequately the diurnal cycle and the effects of transient cloudiness (Wilson and Mitchell 1986). For the tropospheric simulations described in this paper, a zonally uniform ozone distribution was prescribed as a function of latitude and height from the observations of McPeters et al. (1984).

Cloudiness can occur in any GCM layer, and can be associated with large-scale saturation, PBL stratocumulus clouds, or the anvils of deep cumuli. When and where cloudiness occurs, it is assumed to fill an entire grid box, for simplicity; no parameterization of subgrid fractional cloudiness is attempted, although work is under way to develop one (Randall 1987). The optical properties assigned to the clouds are described by HRCD.

Stratocumulus clouds are assumed to be present in the PBL whenever the temperature and mixing ratio at the PBL top (as determined by a mixed-layer assumption) correspond to supersaturation, provided that cloud-top entrainment stability does not occur. The presence of the stratocumulus clouds is felt through both the radiation and entrainment parameterizations. The latter takes into account the generation of turbulence kinetic energy through increased buoyancy fluxes associated with phase changes and highly concentrated cloud-top radiative cooling (Lilly 1968). As a result of these cloud-enhanced buoyancy fluxes, the presence of a stratocumulus layer in the PBL tends to favor more rapid entrainment and, therefore, a deeper PBL.

When cloud-top entrainment stability occurs, the PBL is assumed to exchange mass with the free atmosphere. The amount of mass exchanged is that required to remove the supersaturation, or to restore stability, whichever is less. The PBL depth is assumed to remain unchanged during this process, which we refer to as "layer cloud instability" (LCI).

The prescribed boundary conditions of the GCM include realistic topography, and the observed climatological seasonally varying global distributions of sea surface temperature, sea-ice thickness, surface albedo, and surface roughness, as well as seasonally varying

morphological and physiological parameters for the land surface vegetation. The surface albedo of the ocean is zenith-angle dependent, following Briegleb et al. (1986), who used the data of Payne (1972).

The albedo of the vegetated land surface is determined according to the method of Sellers et al. (1986, appendix B), which includes the effects of snow cover. The fraction of the ground covered by snow is not permitted to exceed 0.8. The albedo of sea ice is 0.8 in the visible, and 0.4 in the near infrared, except that when the temperature of the sea ice is within 0.05 K of the melting point, these values are replaced by 0.48 and 0.24, respectively. The albedo of land ice is 0.8 in the visible and 0.5 in the near infrared.

Simply by recompiling and setting logical switches, the GCM can be run as a one-dimensional model, or as a limited-area model, or as a shallow-water model. "Large-scale" pressure gradients and divergences can be imposed in the one-dimensional and limited-area models. The one-dimensional model is particularly useful for debugging new parameterizations, and for noninteractive sensitivity tests.

The model has a very comprehensive set of diagnostics, which fall into two categories. The first consists of time means of two-dimensional and three-dimensional fields. Most of these fields are sampled every "physics" time step (nominally once per hour), but the surface fluxes and a few others are sampled every "dynamics" step. The time-averaging interval is variable, but is nominally one day. Because the three-dimensional model fields are defined on sigma-surfaces that move as the PBL depth changes, it is necessary to interpolate onto isobaric surfaces before attempting meteorological analysis. This interpolation is done as the model runs, before time-averaging.

The second category of diagnostics consists of high-time-resolution data (nominally sampled once per hour) for selected grid columns. These columns can be chosen without any restrictions, except that if there are too many the model will run noticeably slower and an excessive number of tapes will be generated; we normally use less than 100 columns.

For further detailed description of the GCM see Suarez et al. (1983, and references therein), Harshvardhan et al. (1987), and Randall et al. (1988).

REFERENCES

Ackerman, T. P., K.-N. Liou, F. P. J. Valero and L. Pfister, 1988: Heating rates in tropical anvils. *J. Atmos. Sci.*, **45**, 1606–1623.

Arakawa, A., 1975: Modeling clouds and cloud processes for use in climate models. *The Physical Basis of Climate and Climate Modelling*, GARP Publ. Ser. No. 16, 181–197.

——, and W. H. Schubert, 1974: The interaction of a cumulus cloud ensemble with the large-scale environment. Part I: *J. Atmos. Sci.*, **31**, 674–701.

——, and J.-M. Chen, 1987: Closure assumptions in the cumulus parameterization problem. *Short and Medium Range Numerical Weather Prediction*, Collection of Papers Presented at the *WMO/IUGG Symp. on Numerical Weather Prediction*, Tokyo.

Barkstrom, B. R., 1984: The Earth Radiation Budget Experiment (ERBE). *Bull. Amer. Meteor. Soc.*, **65**, 1170–1185.

Briegleb, B. P., P. Minnis, V. Ramanathan and E. Harrison, 1986: Comparison of regional clear-sky albedos inferred from satellite observations and model computations. *J. Climate Appl. Meteor.*, **25**, 214–226.

Harshvardhan, R. Davies, D. A. Randall and T. G. Corsetti, 1987: A fast radiation parameterization for general circulation models. *J. Geophys. Res.*, **92**, 1009–1016.

——, D. A. Randall, T. G. Corsetti and D. A. Dazlich (HRCD), 1989: Earth radiation budget and cloudiness simulations with a general circulation model. *J. Atmos. Sci.*, **46**, 1922–1942.

Hayashi, Y., and A. Sumi, 1986: The 30–40 day oscillation in an "Aqua Planet" model. *J. Meteor. Soc. Japan*, **64**, 451–466.

Heymsfield, A. J., and K. M. Miller, 1988: Water vapor and ice mass transported into the anvils of CCOPE thunderstorms: Comparison with storm influx and rainout. *J. Atmos. Sci.*, **45**, 3501–3514.

Houze, R. A., 1977: Structure and dynamics of a tropical squall-line system. *Mon. Wea. Rev.*, **105**, 1540–1567.

——, 1982: Cloud clusters and large scale vertical motions in the tropics. *J. Meteor. Soc. Japan*, **60**, 396–410.

Krishnamurti, T. N., D. K. Osterhof and A. V. Mehta, 1988: Air–sea interaction on the time scale of 30 to 50 days. *J. Atmos. Sci.*, **45**, 1304–1322.

Lilly, D. K., 1968: Models of cloud-topped mixed layers under a strong inversion. *Quart. J. Roy. Meteor. Soc.*, **94**, 292–309.

Lord, S. J., W. C. Chao and A. Arakawa, 1982: Interaction of a cumulus cloud ensemble with the large-scale environment. Part IV: The discrete model. *J. Atmos. Sci.*, **39**, 104–113.

Lorenz, E. N., 1967: The nature and theory of the general circulation of the atmosphere. World Meteorological Organization, Geneva, No. 218, TP115, 161 pp.

McPeters, R. D., D. F. Heath and P. K. Bhartia, 1984: Average ozone profiles for 1979 from the Nimbus-7 SBUV instrument. *J. Geophys. Res.*, **89**, 5199–5214.

Moeng, C.-H., and D. A. Randall, 1982: The radiative impact of cumulus cloudiness in a general circulation model. NASA Tech. Memo. 84962, 19 pp.

Payne, R. E., 1972: Albedo of the sea surface. *J. Atmos. Sci.*, **29**, 959–970.

Prabhakara, C. P., D. A. Short and B. E. Vollmer, 1985: El Niño and atmospheric water vapor: Observations from Nimbus 7 SMMR. *J. Climate Appl. Meteor.*, **24**, 1311–1324.

Ramanathan, V., 1987: The role of Earth radiation budget studies in climate and general circulation research. *J. Geophys. Res.*, **92**, 4075–4095.

——, E. J. Pitcher, R. C. Malone and M. L. Blackmon, 1983: The response of a spectral general circulation model to refinements in radiative processes. *J. Atmos. Sci.*, **40**, 605–630.

Randall, D. A., 1980: Conditional instability of the first kind, upside-down. *J. Atmos. Sci.*, **37**, 125–130.

——, J. A. Abeles and T. G. Corsetti, 1985: Seasonal simulations of the planetary boundary layer and boundary-layer stratocumulus clouds with a general circulation model. *J. Atmos. Sci.*, **42**, 641–676.

——, P. J. Sellers and D. A. Dazlich, 1988: Rapid deepening and shallowing in a bulk boundary layer model. Atmospheric Science Paper No. , Colorado State University, in press.

Rood, R. B., 1987: Numerical advection algorithms and their role in atmospheric transport and chemistry models. *Rev. Geophys.*, **25**, 71–100.

Rutledge, S. A., and R. A. Houze, Jr., 1987: A diagnostic modeling study of the trailing stratiform region of a midlatitude squall line. *J. Atmos. Sci.*, **44**, 2640–2656.

Schiffer, R. A., and W. B. Rossow, 1983: The International Satellite

Cloud Climatology Project (ISCCP): The first project of the World Climate Research Programme. *Bull. Amer. Meteor. Soc.*, **64,** 779–784.

Schlesinger, M. E., and J. F. B. Mitchell, 1987: Climate model simulations of the equilibrium climatic response to increased carbon dioxide. *Rev. Geophys.*, **25,** 760–798.

Sellers, P. J., Y. Mintz, Y. C. Sud and A. Dalcher, 1986: A simple biosphere model (SiB) for use within general circulation models. *J. Atmos. Sci.*, **43,** 505–531.

Slingo, A., and J. M. Slingo, 1987: The response of a general circulation model to cloud longwave radiative forcing. Part I: Introduction and initial experiments. *Quart. J. Roy. Meteor. Soc.*, in press.

Starr, D. O'C., and S. K. Cox, 1985a: Cirrus clouds. Part I: A cirrus cloud model. *J. Atmos. Sci.*, **42,** 2663–2681.

——, and ——, 1985b: Cirrus clouds. Part II: Numerical experiments on the formation and maintenance of cirrus. *J. Atmos. Sci.*, **42,** 2682–2694.

Suarez, M. J., A. Arakawa and D. A. Randall, 1983: Parameterization of the planetary boundary layer in the UCLA general circulation model: Formulation and results. *Mon. Wea. Rev.*, **111,** 2224–2243.

Tiedke, M., 1985: Effect of physical parameterization on the large-scale flow in the ECMWF model. *Seminar on Physical Parameterization for Numerical Models of the Atmosphere,* Reading, U.K., European Centre for Medium Range Weather Forecasts, 277–314.

Trenberth, K., 1981: Seasonal variations in global sea level pressure and the total mass of the atmosphere. *J. Geophys. Res.*, **86,** 5236–5246.

Webster, P. J., and G. L. Stephens, 1980: Tropical upper tropospheric extended clouds: Inferences from Winter MONEX. *J. Atmos. Sci.*, **37,** 1521–1541.

Wetherald, R. T., and S. Manabe, 1988: Cloud feedback processes in a general circulation model. *J. Atmos. Sci.*, **45,** 1397–1415.

Wilson, C. A., and J. F. B. Mitchell, 1986: Diurnal variation and cloud in a general circulation model. *Quart. J. Roy. Meteor. Soc.*, **112,** 347–409.